NASA CR-187097

NASA

PLASMA CONTACTOR RESEARCH - 1990

Prepared for

LEWIS RESEARCH CENTER

NATIONAL AERONAUTICS AND SPACE ADMINISTRATION

Grant NAG 3-776

Annual Report

John D. Williams

January 1991

Approved by

Paul J. Wilbur
Department of Mechanical Engineering
Colorado State University
Fort Collins, Colorado 80523

NASA
National Aeronautics and Space Administration

Report Documentation Page

1. Report No.	2. Government Accession No.	3. Recipient's Catalog No.
NASA CR-187097		

4. Title and Subtitle	5. Report Date
Plasma Contactor Research - 1990	Jan. 1990
	6. Performing Organization Code

7. Author(s)	8. Performing Organization Report No.
John D. Williams Paul J. Wilbur	10. Work Unit No.

9. Performing Organization Name and Address	11. Contract or Grant No.
Department of Mechanical Engineering Colorado State University Fort Collins, CO 80523	13. Type of Report and Period Covered Annual Jan. 1, 1989 - Jan. 1, 1990

12. Sponsoring Agency Name and Address	14. Sponsoring Agency Code
National Aeronautics and Space Administration Washington, D.C. 20546	

15. Supplementary Notes

Grant Monitor - Joel T. Galofaro
NASA Lewis Research Center
Cleveland, OH 44135

16. Abstract

Emissive and Langmuir probes were used to measure plasma potential profiles, plasma densities, electron energy distributions and plasma noise levels near a hollow cathode-based plasma contactor emitting electrons. The effects of electron emission current (100 to 1500 mA) and contactor flowrate (2 to 10 sccm [Xenon]) on these data are examined. Retarding potential analyzer (RPA) measurements showing that high energy ions generally stream from a contactor along with the electrons being emitted are also presented and a mechanism by which this occurs is postulated. This mechanism, which involves a high rate of ionization induced between electrons and atoms flowing together from the hollow cathode orifice, results in a region of high positive space charge and high positive potential. Langmuir and RPA probe data suggest that both electrons and ions expand spherically from this potential hill region. In addition to experimental observations, a simple one-dimensional model which describes the electron emission process and predicts the phenomena just mentioned is presented and is shown to agree qualitatively with these observations.

Experimental results of the first stage of bi-lateral cooperation with the Italian Institute of Interplanetary Space Physics (IFSI-CNR) are presented. Sharp, well-defined double layers were observed downstream of a contactor collecting electrons from an ambient plasma created in the IFSI facility. The voltage drop across these double layers was observed to increase with the current drawn from the ambient plasma. This observation, which had not been as clear in previous IFSI tests conducted at higher neutral pressures, is in agreement with previous experimental observations made at both Colorado State University and NASA Lewis Research Center. Greater double layer voltage drops, multiple double layers and higher noise levels in the region near the double layers were also observed when a magnetic field was imposed and oriented perpendicular to the line joining the contactor and simulator.

17. Key Words (Suggested by Author(s))	18. Distribution Statement
Hollow Cathode Plasma Contactor	Unclassified-Unlimited

19. Security Classif. (of this report)	20. Security Classif. (of this page)	21. No of pages	22. Price*
Unclassified	Unclassified	87	

NASA FORM 1626 OCT 86

*For sale by the National Technical Information Service, Springfield, Virginia 22161

TABLE OF CONTENTS

LIST OF FIGURES

LIST OF TABLES

Nomenclature

$B_{//}$ Axial magnetic field strength--component along the line joining the contactor and the simulator (G)

$B_{\perp}$ Transverse magnetic field strength--component perpendicular to the line joining the contactor and the simulator (G)

e Magnitude of electronic charge (1.60×10^{-19} C)

J_{CD} Contactor discharge current (A)

J_{CE} Electron current emitted by contactor (A)

J_p Ion current at r_e due to ions produced between r_e and r_B which flows from the potential hill region to the cathode (A)

J_{SD} Simulator discharge current (A)

J_{SE} Electron current collected by simulator (A)

J_{SF} Simulator filament cathode heating current (A)

J_+ Ion current at r_A due to ions produced between r_B and r_A which flow from the potential hill region to the downstream boundary (A)

j_+ Current density of high energy ions flowing from the vicinity of the contactor to regions downstream of it (A m^{-2})

k Boltzmann's constant (1.38×10^{-23} J K^{-1})

$\dot{m}_c$ Flowrate of neutrals supplied to contactor (sccm [Xe]--standard cubic centimeters per minute)

m_e Mass of electron (9.11×10^{-31} kg)

m_p Mass of ion (xenon: 2.18×10^{-25} kg)

$\dot{n}$ Neutral atom supply rate (from hollow cathode) (s^{-1})

n_e Electron density (m^{-3})

n_o Neutral atom density (m^{-3})

n_p Density of ions on the cathode side of the potential hill [i.e.

those that flow toward the cathode] (m^{-3})

n_+ Density of ions on the downstream side of the potential hill [i.e. those that flow toward the downstream boundary] (m^{-3})

P_o Ambient pressure measured far from the hollow cathode (Pa)

$R(r)$ Volumetric production rate of ions at radius r (s^{-1} m^{-3})

r Radius measured from the hollow cathode (m)

r_1 Radius measured from the hollow cathode (used as a dummy integration variable) (m)

r_A Radial position of the spherical shell at the downstream boundary (i.e. at the base of the potential hill) (m)

r_B Radial position of the potential hill peak (or crest) (m)

r_e Radial position of the spherical shell boundary from which electrons are supplied (m)

T_o Neutral atom temperature measured far from the hollow cathode (K)

V Potential measured with respect to (wrt) the contactor cathode (V)

V_A Potential at r_A (wrt contactor cathode) (V)

V_B Potential at r_B, crest potential (wrt contactor cathode) (V)

V_C Bias supply voltage (wrt contactor cathode) (V)

V_{CD} Contactor discharge voltage, downstream boundary potential (wrt contactor cathode) (V)

V_{SD} Simulator discharge voltage (wrt simulator cathode) (V)

v_e Electron velocity (m s^{-1})

v_{oc} Velocity of neutrals flowing from the hollow cathode (m s^{-1})

Z Axial position measured from the contactor cathode along the tank/contactor centerline (m)

Greek symbols:

ε_o Permittivity of free space (8.85×10^{-12} F m^{-1})

ψ Solid angle of the spherical sector through which electron emission occurs (steradian)

ψ_o Solid angle of the spherical sector through which neutral atoms expand as they exit the orifice of the hollow cathode (steradian)

σ_+ Electron/Neutral atom ionization cross-section (m^2)

Langmuir Probe Analysis Variables and Definitions:

A_p Surface area of spherical Langmuir probe- CSU probe: 3.1×10^{-5} m^2, IFSI probe: 2.8×10^{-5} m^2

E Electron energy (eV)

E_p Primary (or mono-energetic) electron energy (eV)

F(E) Electron energy distribution function (Normalized)

J_{sat} Electron current flowing to a 3.1 mm dia., spherical Langmuir probe being held at plasma potential (A)

n_e Maxwellian electron density (cm^{-3})

n_p Primary (or mono-energetic) electron density (cm^{-3})

T_e Maxwellian electron temperature (eV)

$V_{P,EP}$ Plasma potential measured by emissive probe (V)

$V_{P,LP}$ Plasma potential measured using Langmuir probe and analysis program developed at IFSI by Guidoni et. al. (V)

IFSI Acronym for Istituto di Fisica dello Spazio Interplanetario of the Consiglio Nazionale Delle Ricerche of Italy

CSU Acronym for Colorado State University

LeRC Acronym for Lewis Research Center of the National Aeronautics and Space Administration

ELECTRON EMISSION FROM A HOLLOW CATHODE-BASED PLASMA CONTACTOR

Introduction

Several experimental [1,2,3] and theoretical studies [4,5,6] have focused on the problem of controlling spacecraft electric potential with respect to an adjacent environment using plasma producing devices. These particular studies involved electrodynamic tether applications in which the plasma producing devices provide relatively high current capacity "contacts" to plasmas at each end of the tether. Most of this work concentrated on the processes that occur at the positively biased "plasma contactor" (i.e. the one collecting electrons from and emitting ions to the space plasma); and little attention was given to the negatively biased contactor that emits electrons. This study addresses this deficiency by focusing on the processes that occur near a plasma contactor emitting electrons to a simulated space plasma in a laboratory environment. The plasma contactor used in these experiments is a hollow cathode--a device derived from ion thruster neutralization applications. The hollow cathode plasma source is particularly well suited to charge control applications because of its robust construction and long lifetime characteristics, high electron emission current capabilities (in excess of 60 A [7]), and capacity to produce a cool, neutral plasma.

Observations of the particles coming from a contactor emitting electrons made using a retarding potential analyzer (RPA) show that relatively high energy ions stream away along with the electrons being emitted. A mechanism is postulated in this report that could explain this observation. An important part of the mechanism is the high rate of ionization that occurs when atoms and electrons are expelled simultaneously

through a small orifice as they are in a hollow cathode discharge [7,8]. A similar mechanism for the creation of high energy ions has also been proposed by investigators [9,10] studying various electric arcs. A plasma contactor operating in this manner (emitting both ions and electrons) should be well suited to spacecraft charging control because small changes in the potential difference between the spacecraft and the ambient plasma should cause the currents associated with the ion and electron flow between the contactor and space plasma to be altered. This would be expected in turn to facilitate the changes in current required to prevent the spacecraft from becoming either substantially positive or negative of the plasma surrounding it in a variety of spacecraft charging situations. This work describes recent experimental results obtained on a hollow cathode emitting a net electron current to a surrounding ambient plasma and presents a first order, one-dimensional model of the process.

Apparatus and Procedure

In order to study the electron emission process, the apparatus shown schematically in Fig. 1 was constructed. Physically this apparatus consists of two plasma producing devices. The one shown at the right and labeled "simulator" generates a simulated ionospheric plasma. The other device, shown on the left and labeled "plasma contactor", is the focus of this study and is biased negative relative to the ambient plasma to induce electron emission. Also shown are the power supplies and instrumentation needed to sustain and measure the characteristics of the plasmas produced. The simulator and contactor devices are separated by 2.7 m and are located within a 1.2 m dia. by 5.3 m long vacuum chamber. The contactor utilizes a 6.4 mm dia. hollow cathode that contains an electron emitting insert fabricated by rolling 0.013 mm thick tantalum foil into the shape of a hollow cylinder and treating it with a low

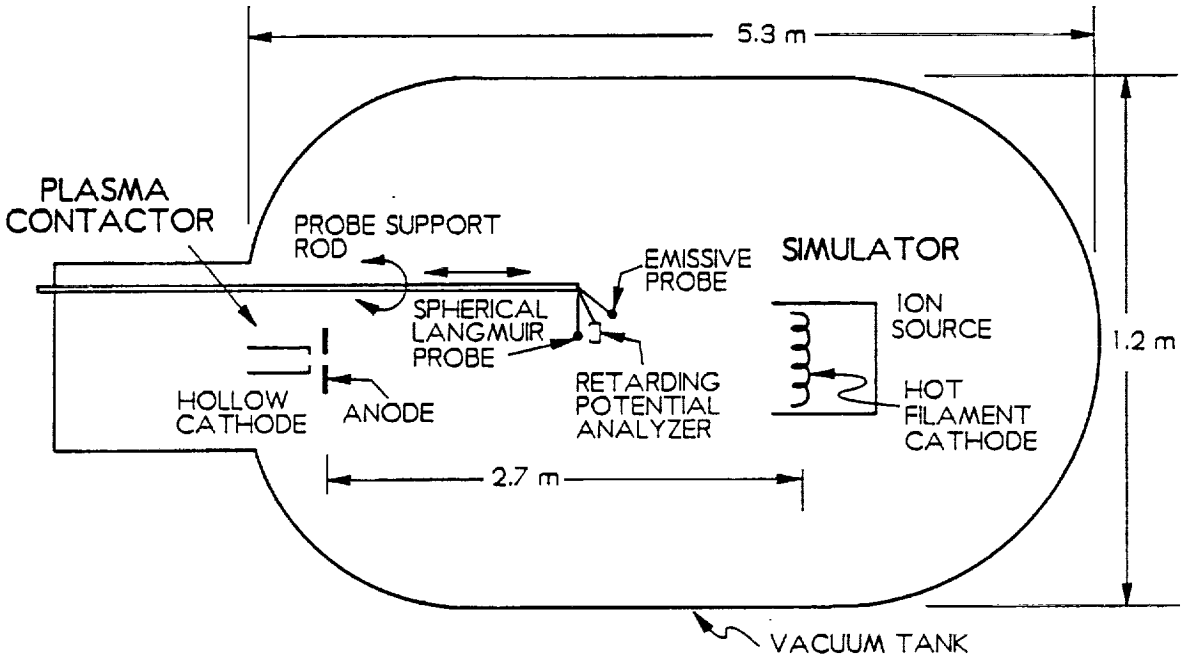

a. Mechanical Schematic

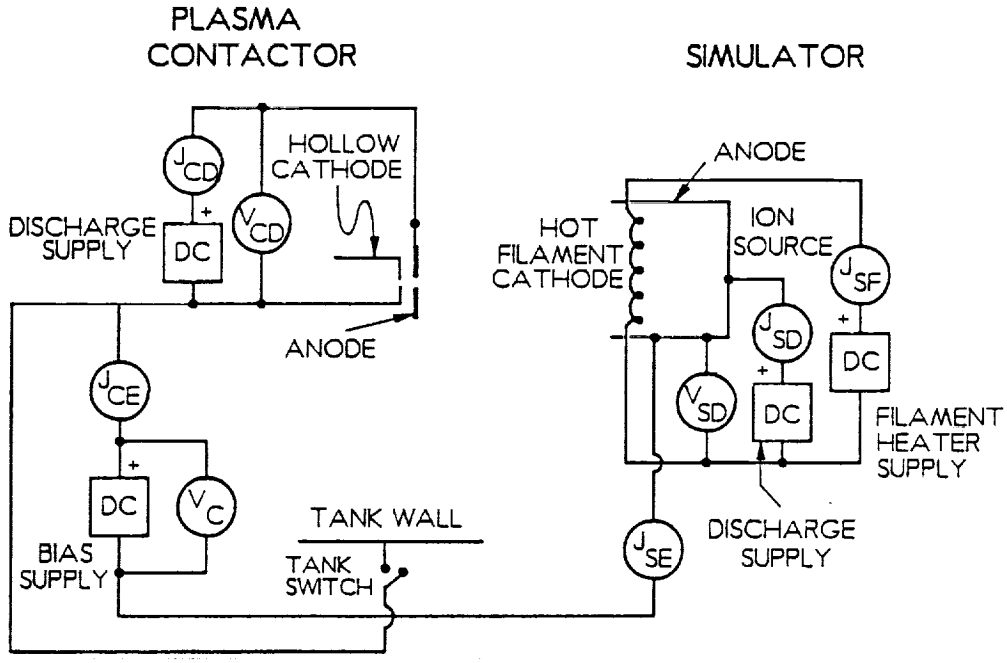

b. Electrical Schematic

Fig. 1 Experimental Apparatus

work function coating (containing a double carbonate [$BaCO_3$, $SrCO_3$]). An orifice plate with a 1.0 mm dia. orifice caps the downstream end of the hollow cathode tube. The contactor anode is a 12 cm dia. stainless steel plate with a 1 cm O.D./5 mm I.D. tantalum insert near its center. The tantalum anode insert is aligned with the hollow cathode orifice and positioned $\sim$2 mm downstream of it.

Physically, the simulator resembles a ring-cusp ion source used in ion thruster applications [11]. Plasma is generated within it by collisions between high energy discharge electrons and neutral atoms. In order to increase the efficiency of this process, magnetic fields are used to shield anode surfaces and chamber walls against direct loss of discharge electrons. The ring-cusp magnetic field used in the simulator is induced by samarium cobalt permanent magnets. In order to ensure good coupling between the plasma produced within the source and the ambient plasma region, the device was operated without plasma extraction grids. The simulator is equipped with a tungsten wire cathode which is stretched diagonally across the 9 cm dia. open end of the source. When it is heated to thermionic temperatures it emits electrons that are eventually collected at the simulator body, which serves as the anode for this device as Fig.1b suggests. For most of the experimental results presented in this study, the simulator discharge current and voltage were set at 0.5 A and 40 V, respectively, and the simulator flowrate was set at 2.7 sccm (Xe).

Typical tests were conducted by heating the contactor hollow cathode to a temperature where significant thermionic electron emission could occur from the insert ($\sim$1300 K), establishing a high expellant (xenon) flowrate through it, and biasing its anode positive using the discharge supply to initiate a cathode-to-anode discharge.

Next, the desired contactor flowrate and discharge current were established; the contactor was biased relative to the simulator using the bias power supply; and voltage, current and probing instrument data were collected. The voltages and currents measured during typical tests are designated by the symbols shown within the circles in Fig. 1b and defined in the nomenclature list. These quantities include the contactor and simulator discharge currents and voltages, the bias voltage between the contactor and simulator, and the contactor and simulator electron emission currents.

The tank bias switch shown in Fig. 1b was installed so the vacuum tank could be allowed to float relative to the contactor-simulator system or could be connected to the contactor cathode. Experimental results were typically not affected by the switch position and, consequently, it was left closed for the tests described here. The plasma environment produced between the contactor and the simulator was probed using the various instruments shown in Fig. 1a. They include an emissive probe, a Langmuir probe, and a retarding potential analyzer (RPA). The RPA consists of a cylindrical Faraday cage with an orifice plate at one end--the orifice hole diameter of 3 mm was selected to be smaller than the Debye length of the plasma in which it is typically used. The Faraday cage was held about 40 V below the potential of the plasma in which it was immersed. The probe is operated by first sighting the RPA orifice at the plasma contactor and then recording the ion current to the probe collector as the voltage is swept from 10 V below contactor cathode potential to about 100 V above it. The details of the current/voltage traces obtained and their analysis and interpretation are discussed in Refs. [7] and [12].

Experimental Observations

Some of the phenomena observed in ground-based studies of the process of electron flow from a hollow cathode-based plasma contactor to a low density ambient plasma can be explained using the typical plasma potential profile shown in Fig. 2. In this case the contactor cathode, at zero potential and zero axial position, was emitting 61 mA of electrons into an ambient background plasma located about 1 m downstream of the contactor. A noteworthy feature of this potential profile is the hill structure that develops immediately downstream of the contactor. It is postulated that this potential hill develops as a result of a high rate of ionization at the location of the hill. Because the contactor is emitting both neutrals and electrons (and both have high densities near the contactor), a region where the ionization rate is high can develop. Under this condition, electrons that cause the ionization and the electrons produced would typically be expected to have substantial kinetic energies after the ionization event, and they would be expected to leave the region quickly. However, the more massive ions would be left behind thereby creating a region in which the ion density is greater than the electron density. This net positive space-charge density region would induce a potential hill like the one shown in Fig. 2. It should be noted that the plasma potential data shown in Fig. 2 were obtained using a floating emissive probe, and these probes indicate potentials that fall progressively further below true plasma potential as they are moved into higher density plasmas [13]. Because plasma density is greatest at the hollow cathode orifice, the emissive probe probably indicates potentials that fall progressively further below true values as the cathode is approached at $Z=0$. Hence,

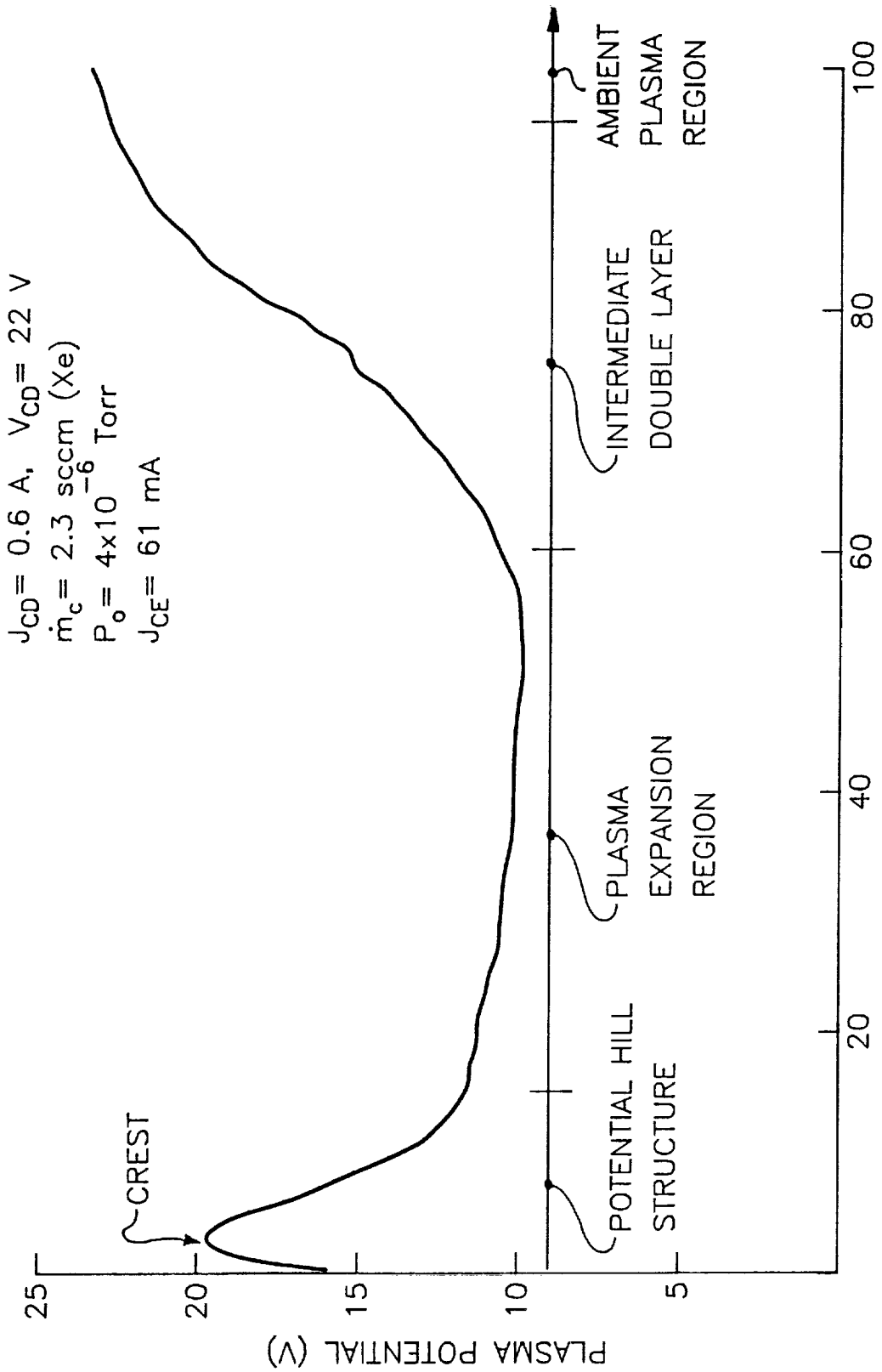

Fig. 2 Plasma Potential Profile on the Contactor/Vacuum Tank Centerline (Contactor Emitting Electrons)

it is possible that the true crest of the hill is higher and located at a different axial position than the one indicated in Fig. 2.

Downstream of the potential hill, Fig. 2 shows that the plasma potential is relatively constant from 15 to 60 cm. This region is called the plasma expansion region because the plasma density decreases in proportion to Z^{-2} there and this in turn suggests a region of spherical plasma expansion [1]. Generally it appears that the plasma overexpands in this region. This is demonstrated by Langmuir probe data [1] which show that the plasma density at the downstream end of the plasma expansion region is below that of the ambient plasma region (the region of constant plasma potential extending beyond 100 cm in Fig. 2). It appears that the intermediate double layer (shown between 60 and 100 cm) enables accommodation of this difference in plasma densities. These phenomena and double layers in general are discussed in more detail by Hershkowitz [14] and the references therein. The criteria that determine the location, geometry and size of the intermediate double layer probably depend upon the ion creation and loss rates in the ambient and expanding plasma regions, the ion and electron current densities, and interactions with the vacuum test facility walls. However, the details of its characteristics have not been investigated in this study.

A relatively low flowrate (2.3 sccm [Xe]) and emission current (61 mA) were selected for the measurements of Fig. 2 because these operating conditions yielded a sufficiently low plasma density near the cathode so the potential hill could be detected using an emissive probe. As flowrate and/or electron emission current were increased, the potential hill sensed by the probe began to disappear. In order to determine if this was due to emissive probe inadequacy or if it indicated that the height of the potential hill was truly decreasing, an RPA was positioned in the plasma expansion region and

used to measure the energy characteristics of the ions coming from the vicinity of the contactor. Two typical RPA traces (recorded with the RPA positioned at Z=20 cm and sighted at the contactor cathode) along with their corresponding derivatives are shown in Fig. 3. These data were obtained with the contactor operating at a high flowrate (9.6 sccm [Xe]) where emissive probe measurements showed no evidence of potential hills at either the 130 or 1000 mA electron emission levels. The RPA curve and corresponding derivative for the high emission current case (J_{CE}= 1000 mA) indicate that two groups of ions are present. The first group induces the peak occurring near 15 V in the lower plot and represents low energy, thermal ions present in the expanding plasma. The second group which exhibits a greater energy spread is present as the tail on the solid curve extending from 20 to 100 V (Fig. 3b). It is postulated that the high energy ions associated with this tail are created on a potential hill located near the contactor cathode and that they flow from there to the RPA where they are detected. The RPA data corresponding to contactor operation at a low electron emission current of 130 mA displays only one low energy group of ions. This suggests that no potential hill forms at this operating condition.

There are other differences between the plasmas measured in the expanding plasma region at 130 and 1000 mA emission currents and one of these, the difference in electron energy distribution functions sensed by a Langmuir probe, is illustrated in Fig. 4. At a high emission current, the solid curve suggests that two electron groups exist. One group, associated with the lower energy peak, probably represents the thermal electrons present in the expanding plasma. The other, higher energy group is associated with electrons that have been accelerated from the contactor cathode through the potential hill region and into the expanding plasma without experiencing many

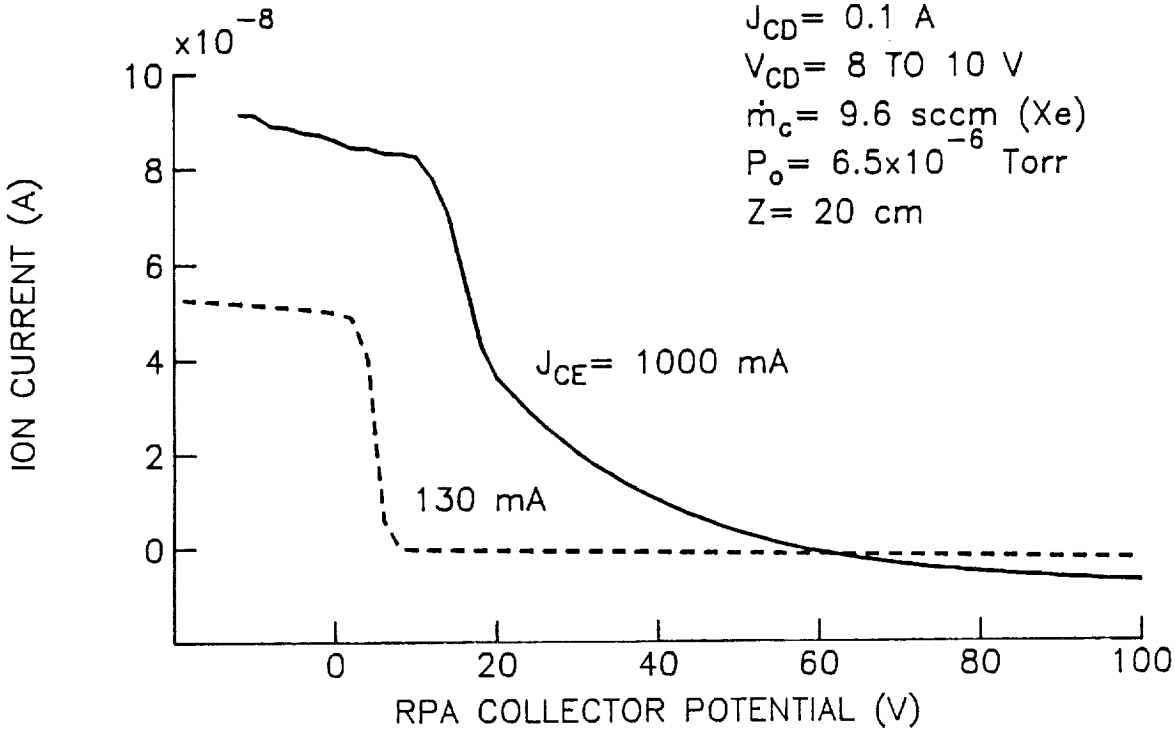

a. Current/Voltage Traces

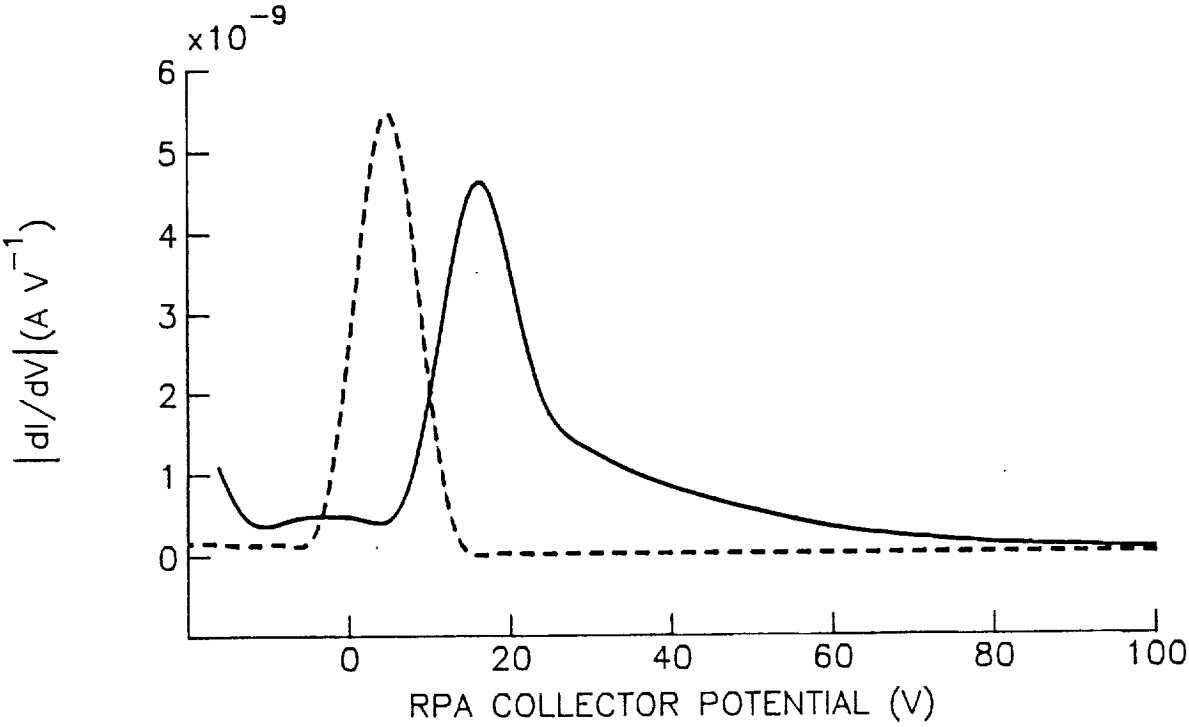

b. Derivatives of Current/Voltage Traces

Fig. 3 Retarding Potential Analyzer Data Measured in the Expanding Plasma Region (High Contactor Flowrate Condition)

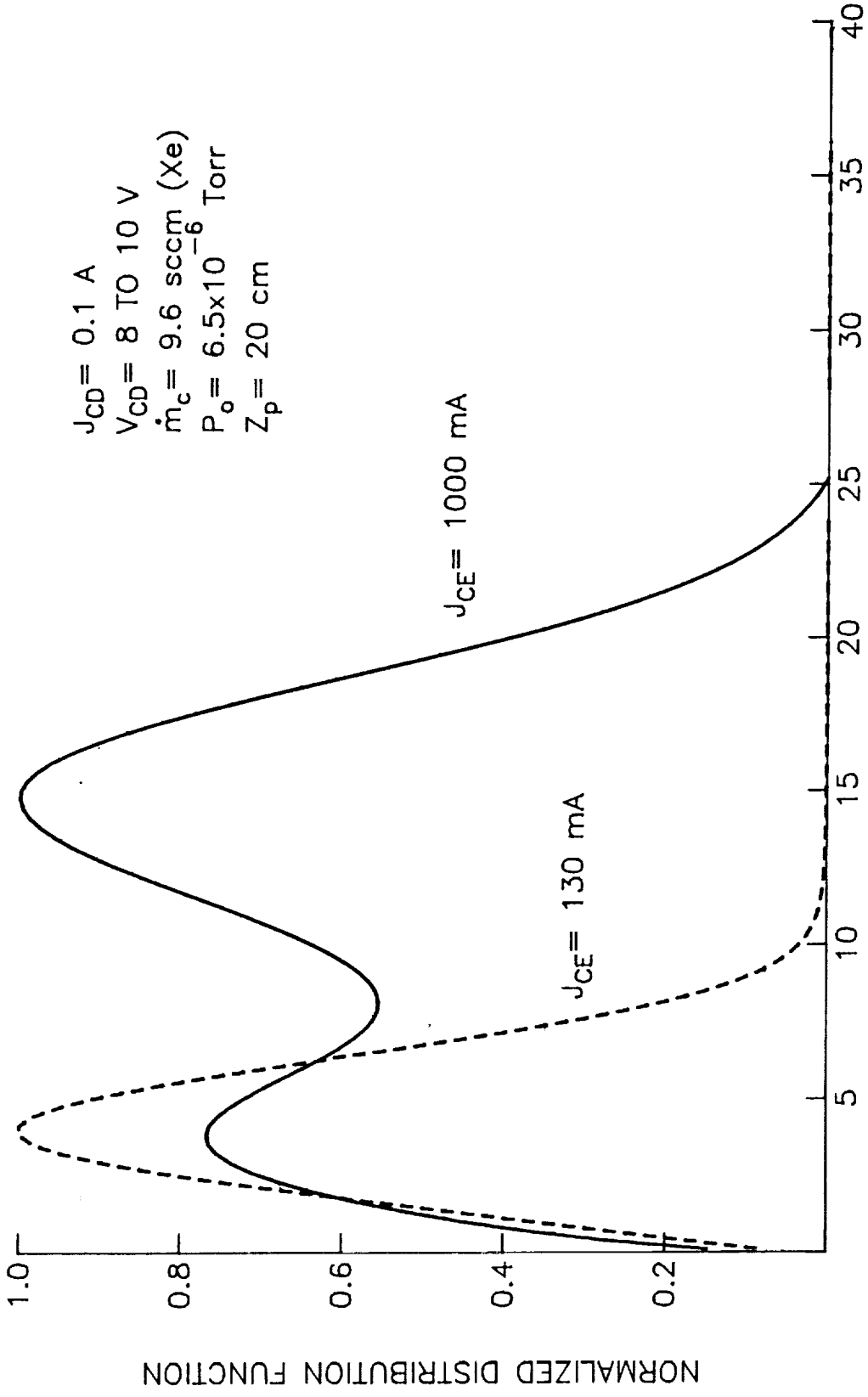

Fig. 4 Electron Energy Distributions Measured in the Expanding Plasma Region (High Contactor Flowrate Condition)

energy dissipating collisions. However, the electron distribution function corresponding to the low emission current condition (J_{CE}=130 mA) indicates only one, low energy group of electrons is present. Thus, Figs. 3 and 4 show that both ions and electrons in the expanding plasma region exhibit distribution functions that have thermal and high energy components at a high emission current, while only the thermal component is present at a lower electron emission current. Note that the electron energy distribution functions shown in Fig. 4 have been normalized with respect to their maxima. They were computed from the second derivatives of spherical Langmuir probe traces recorded digitally using a Keithley 617 programmable electrometer and plasma potential data measured using the emissive probe. The derivatives were obtained by finding the discrete Fourier series representation of the Langmuir probe trace, solving for the analytical derivative of this series and applying a convergence filter [15]. The convergence filter artificially smooths the data and tends to spread out quickly varying features of the Langmuir probe trace. Smoothing errors introduced by the data reduction procedure and plasma potential measurement errors yield distribution functions (Fig. 4) that reflect only the qualitative differences between the plasmas observed at the 130 and 1000 mA operating conditions. Appendix A contains a more detailed explanation of the procedures used to compute electron energy distribution functions, and Appendix B contains an explanation of the technique used to obtain plasma potential using a floating emissive probe.

It is also of interest to examine the effect of electron emission current on the axial profiles of the high energy ion current density and the random electron current. These profiles have been measured over a range of electron emission currents and the results are shown in Fig. 5. The data in this figure correspond to a lower flowrate

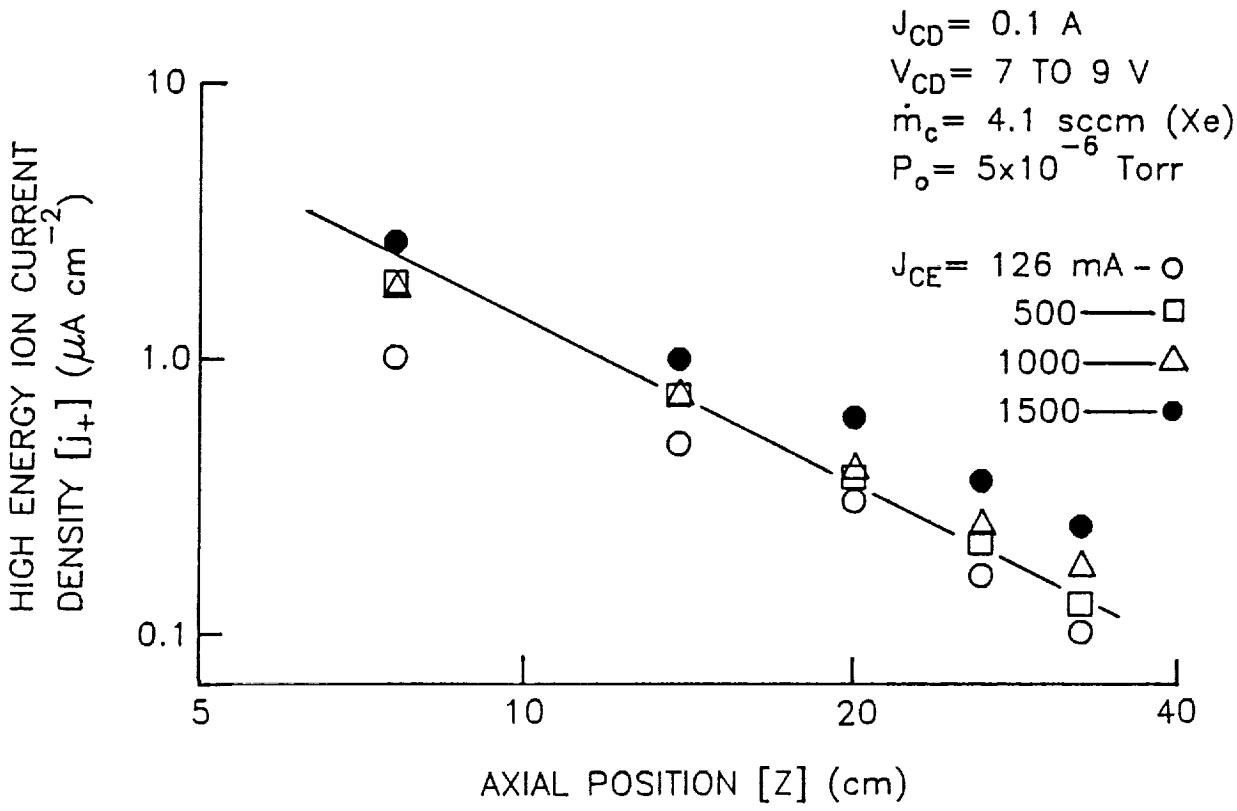

a. Effect of Electron Emission Current on High Energy Ion Current Density Profiles

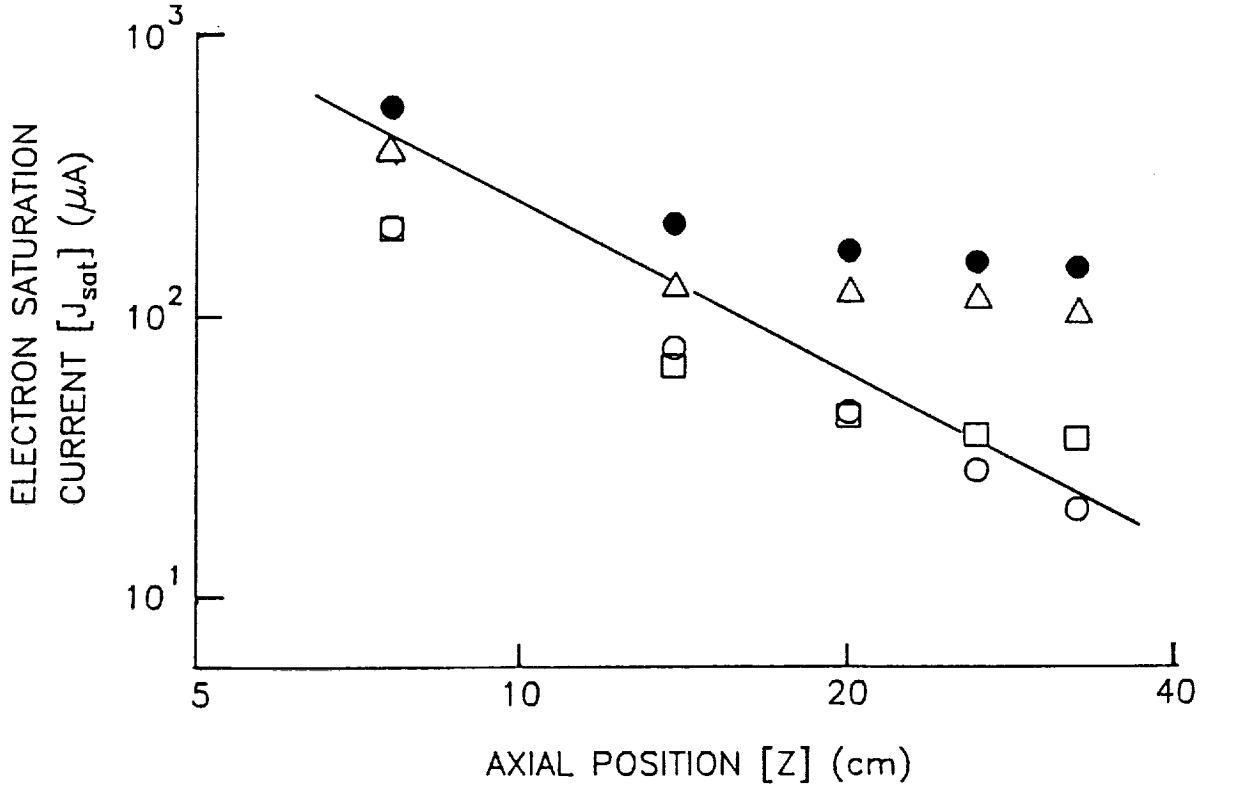

b. Effect of Electron Emission Current on Langmuir Probe Electron Saturation Current Profiles

Fig. 5 Experimental Observations Suggesting Spherical Expansion in the Region Downstream of the Potential Hill Structure

(4.1 sccm [Xe]) than those of Figs. 3 and 4. At this lower flowrate, high energy ions were detected flowing from the contactor at all four of the electron emission current levels shown (i.e. at J_{CE}= 126, 500, 1000 and 1500 mA). The lines drawn on the two plots shown in Fig. 5 correspond to an inverse square dependence with axial position.

The high energy ion current density is shown to follow the inverse square dependence (Fig. 5a) and this suggests that the high energy ions are indeed expanding spherically from their point of creation. On the other hand, the electron saturation current in the expanding plasma region decreases less rapidly than the inverse square of distance--especially at large values of axial position as shown in Fig. 5b. The electron saturation current [J_{sat}] is defined to be the electron current flowing to the Langmuir probe held at plasma potential. Hence this current includes both high energy (beam) electron and thermal electron components. It is considered likely that the data of Fig. 5b do not always follow the Z^{-2} dependence either because the beam electrons are being thermalized or their presence is being masked by thermal electrons in the plasma expansion region.

Both the high energy ion and directed electron populations present in the expanding plasma can contribute to instabilities and cause the expanding plasma to be noisy or turbulent. A coarse measure of the turbulent intensity (the fraction of the energy in the expanding plasma that is in the form of turbulent electrostatic fluctuations) is the square of the ratio of the rms density fluctuations to the mean plasma density. This density ratio can be measured qualitatively in the low density expanding plasma by monitoring the current to a Langmuir probe when it is held near plasma potential and recording the rms noise amplitude/mean current ratio. Figure 6 shows rms-to-mean current ratio versus axial position data corresponding to the data

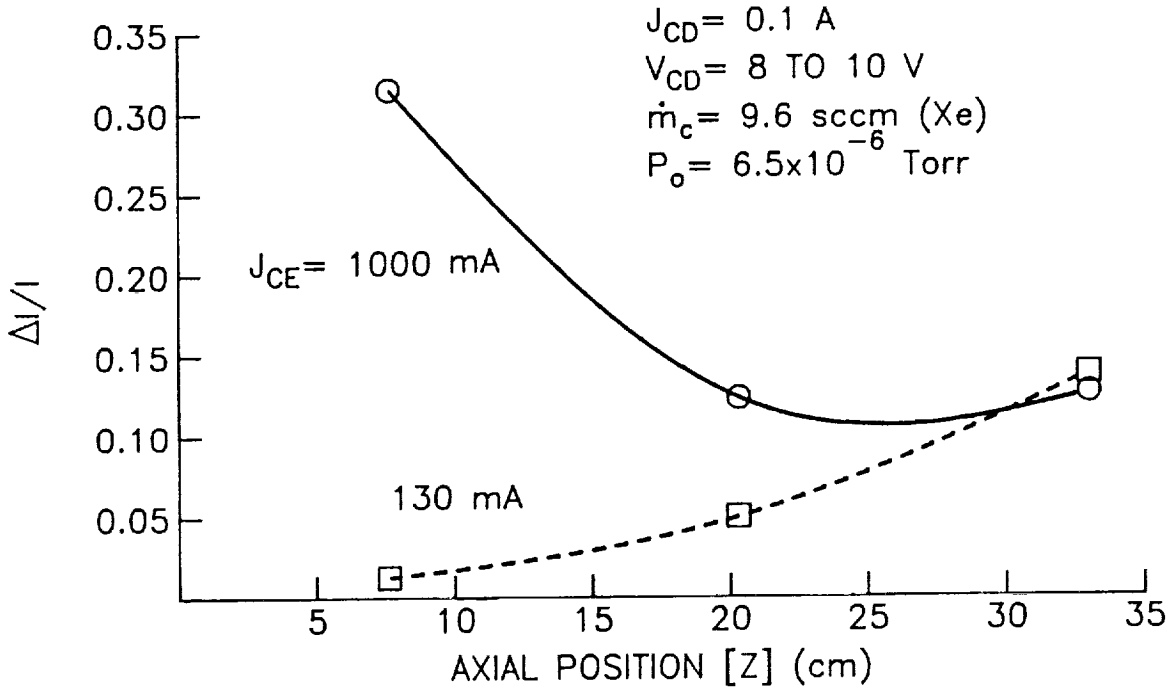

Fig. 6 Langmuir Probe Noise Levels at High and Low Electron Emission Currents (High Contactor Flowrate Condition)

presented in Figs. 3 and 4. The data for the 1000 mA operating condition suggest that the plasma is very noisy near the plasma contactor (turbulent intensity $\sim [0.32]^2 =$ 10%) and less noisy ($\sim$ 2%) at larger axial positions, and the opposite trend is indicated for the 130 mA operating condition. The noise levels at 33 cm are shown to be comparable thereby suggesting that phenomena occurring in the ambient plasma region determine the noise level at axial positions greater than 30 cm.

Theoretical Development

In order to gain some understanding of the potential hills that have been measured at low emission currents and postulated at higher ones, a simple model of the electron emission process has been developed. Figure 7 is a sketch of the spherical geometry associated with a hypothetical potential profile that shows the electron emission current J_{CE} flowing from the hollow cathode through the potential hill to a downstream boundary. As these electrons leave the electron source surface, they are accelerated up the potential hill and they gain sufficient energy to ionize neutral atoms. The resulting ions will flow down the hill from the point where they were produced. Ions produced to the left of the crest potential shown in Fig. 7 will flow to the cathode and those produced to the right of it will flow to the downstream boundary. The streaming electrons, which accelerate to the crest and then decelerate after they pass it, will still have substantial kinetic energies as they pass the downstream boundary.

The approach used here will be to write equations that describe the electron and ion densities throughout the region between the electron source and the downstream boundary and then apply Poisson's equation to solve for the associated potential profile. Because the electron and ion densities depend upon the potential profile, however, an iterative solution technique must be applied to accomplish this and obtain the

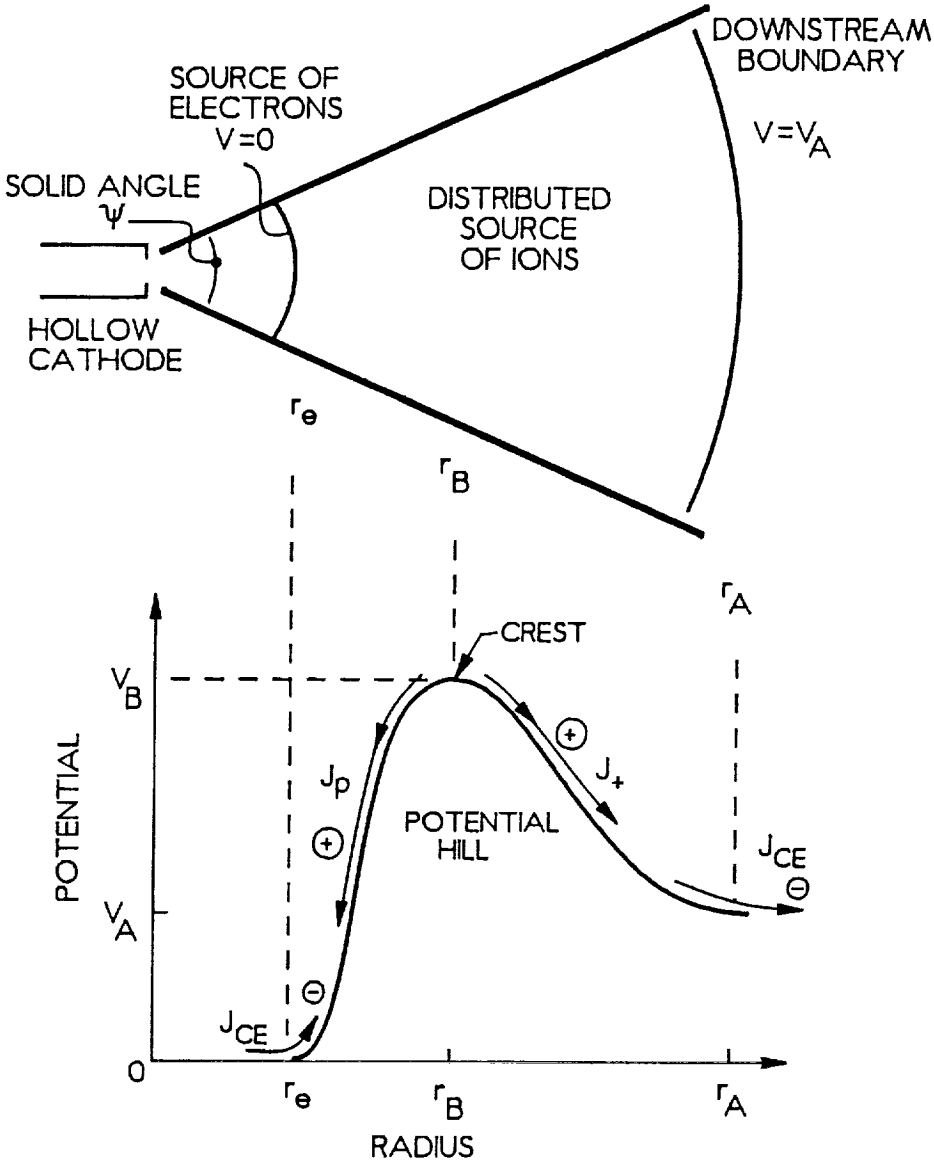

Fig. 7 Spherical Model Diagram of the Electron Emission Process

steady-state, self-consistent solution for the density and potential profiles. This model of the electron emission process will be presented in terms of two sets of equations. One set will pertain to radial locations between the cathode and the potential peak (i.e. on the cathode side of the potential hill). The other set will pertain to radial locations between the potential hill and the downstream boundary (i.e. on the downstream boundary side).

The Cathode Side ($r_e < r < r_B$)

The electron density at any point in this region can be described approximately by assuming conservation of electron energy and current,

i.e.

$$\frac{1}{2} m_e [v_e(r)]^2 = e V(r) \qquad (1)$$

and

$$J_{CE} = e n_e(r) \psi r^2 v_e(r) \qquad . \quad (2)$$

Combining these equations and solving for the electron density gives

$$n_e(r) = \frac{J_{CE}}{e \psi r^2} \sqrt{\frac{m_e}{2eV(r)}} \qquad . \quad (3)$$

This expression for the electron density is only approximately correct because it ignores both electrons which are produced in ionization events and the effects of energy removal from the electron group due to ionization and other inelastic collisions. Neglecting these effects to make the problem more tractable limits its direct applicability to the case where the inelastic collision rate expressed as a current is small compared to the electron emission current. It is assumed that some mechanism for

removing low energy electrons produced via ionization from the potential hill region is active. Although this mechanism is not defined, it is noted that the current of these electrons should be small so a negligible fraction of the kinetic power in the streaming electrons would be required to remove them through elastic collisions.

The rate of ion generation per unit volume [R(r)] at radius r is given by

$$R(r) = n_e(r)\ n_o(r)\ \sigma_+(v_e)\ v_e(r) \quad . \quad (4)$$

The ionization cross-sections of Rapp and Englander-Golden [16] were used to calculate ion generation rates. In addition, the neutral atom density n_o appearing in this equation is assumed to be the sum of the neutral densities due to the neutral flow from the hollow cathode (assumed to expand spherically from the orifice) and the background neutral density in the vacuum environment of the test. Specifically, the density n_o at radius r was approximated by

$$n_o(r) = \frac{\dot{n}}{\psi_o\ r^2\ v_{oc}} + \frac{P_o}{k\ T_o} \quad . \quad (5)$$

The density of ions at a radius r is determined by summing the contributions of all ions produced at radii of greater potential. Each of these ions will be accelerated from their point of creation r_1 to the radius of interest r. Hence, the contribution to the density of ions at a radial location r (for the region $r_e < r < r_B$) due to ions generated with a negligible initial velocity in a differential volume near r_1 is

$$dn_p(r) = r^{-2}\ \frac{R(r_1)\ r_1^2\ dr_1}{v(r_1)} \quad . \quad (6)$$

and the velocity of the ions created at r_1 once they reach r is given by

$$v(r_1) = \sqrt{\frac{2e[V(r_1)-V(r)]}{m_p}} \quad . \quad (7)$$

The overall ion density at any radius r on the cathode side of the hill is now found by integrating the differential density dn_p from r to r_B. This yields

$$n_p(r) = r^{-2} \int_r^{r_B} \frac{R(r_1)\, r_1^2\, dr_1}{v(r_1)} \quad . \quad (8)$$

Combining Eqs. 3 through 8 and simplifying gives

$$n_p(r) = r^{-2}\, \frac{J_{CE}\sqrt{m_p}}{\sqrt{2}\ \psi\ e^{3/2}} \int_r^{r_B} \left[\frac{\dot{n}}{\psi_o r_1^2 v_{oc}} + \frac{P_o}{k\ T_o} \right] [V(r_1)-V(r)]^{-1/2} \sigma_+\, dr_1 \quad (9)$$

The electron and ion densities determined using Eqs. 3 and 9 can now be combined with Poisson's equation to describe the variation in plasma potential on the cathode side of the potential hill. Assuming spherical symmetry, Poisson's equation is

$$\frac{d^2V}{dr^2} + \frac{2}{r}\frac{dV}{dr} = \frac{e}{\varepsilon_o}\left(n_e(r) - n_p(r)\right) \quad . \quad (10)$$

In order to apply the equations just developed, it is necessary to develop the equations describing conditions on the opposite (downstream boundary) side of the potential hill so all of them can be solved simultaneously.

The Downstream Boundary Side ($r_B < r < r_A$)

Under the assumptions of this development, the equation that describes the electron density in the region between the potential crest and the downstream boundary is the same as the one developed for application upstream of the potential crest, namely Eq. 3. The ion density expression is obtained by repeating the logical sequence used to derive Eq. 9. It is found to differ from Eq. 9 only in the order of the integration, hence

$$n_+(r) = r^{-2} \frac{J_{CE}\sqrt{m_p}}{\sqrt{2}\ \psi\ e^{3/2}} \int_{r_B}^{r} \left[\frac{\dot{n}}{\psi_o r_1^2 v_{oc}} + \frac{P_o}{k\ T_o} \right] [V(r_1)-V(r)]^{-1/2}\ \sigma_+ dr_1 \quad (11)$$

Note that Eq. 11 shows an inverse square dependence with position and a linear dependence with emission current. This is in qualitative agreement with the functional dependencies indicated by the experimental data of Fig. 5a.

Equations 3, 9, 10, and 11 represent a relatively simple model of the electron emission process. They were solved by first dividing up the region r_e to r_A using small, evenly-spaced node points. Next, the derivatives in Eq. 10 were approximated using finite-difference expressions. This allowed algebraic equations arranged in matrix form to be written for the potential at each node point. Electron and ion densities were then calculated at each node point using Eqs. 3, 9 and 11 and an initial estimate of the potential variation through the potential hill region. The procedure of solving for the densities and then the potentials at each node was repeated many times until the potential profile stabilized.

It should be noted that the solution procedure treats 1) the electron source location r_e, 2) the downstream boundary location r_A, 3) the solid angles ψ and ψ_o, and

4) the potential at the downstream boundary V_A as parameters. The electron source and downstream boundary locations are, however, not free parameters. The values of r_e and r_A are established physically by the requirement that the electric fields be zero at these locations (i.e. the space-charge limited condition applies). It was postulated that the other parameters, namely the downstream boundary potential V_A, and the solid angles ψ and ψ_o were influenced by such factors as the cathode orifice size, the anode configuration, and the plasma conditions beyond the downstream boundary and they were treated as free parameters. It is believed that an energy balance analysis could be used to find the downstream boundary potential, but this was not accomplished in this preliminary study. In order to apply the model and compare its predictions to experimental observations, V_A was set at the experimentally measured potential in the expanding plasma region (typically measured at a radius of 20 cm) for each electron emission operating condition studied. The solid angles ψ and ψ_o were arbitrarily set to 2π (i.e. hemispherical geometry). There are other parameters appearing in equations 3, 9, 10, and 11 that are not determined explicitly through the analysis (e.g. P_o and T_o), but they were controlled during the experiment and unique values could be assigned to them.

Numerical Example

When Eqs. 3, 9, 10, and 11 were solved for the case of an emission current of 1 A and values of the parameters given in Table 1, the theoretical potential profile shown in Fig. 8a was computed. By forcing the boundary electric fields to be zero, the electron source and downstream boundaries were found to be located at 4.6 and 14.4 mm, respectively, and the crest potential of 153 V was located at 7.4 mm. This large potential was caused by a net positive (ion) charge density in the region between

Table 1 Numerical Example Data Set

Inputs	Outputs
J_{CE} = 1.0 A	Fig. 8
$\dot{m}_c$ = 4.1 sccm (Xe) (or $\dot{n}$ = 1.72×10^{18} s^{-1})	J_+ = 1.94 mA
	J_p = 2.16 mA
P_o = 5.0×10^{-6} Torr (or 6.7×10^{-4} Pa)	r_e = 4.6 mm
T_o = 300 K	r_B = 7.4 mm
v_{oc} = 458 m s^{-1}	r_A = 14.4 mm
$\psi = 2\pi$	V_B = 153 V
$\psi_o = 2\pi$	
V_A = 22 V	

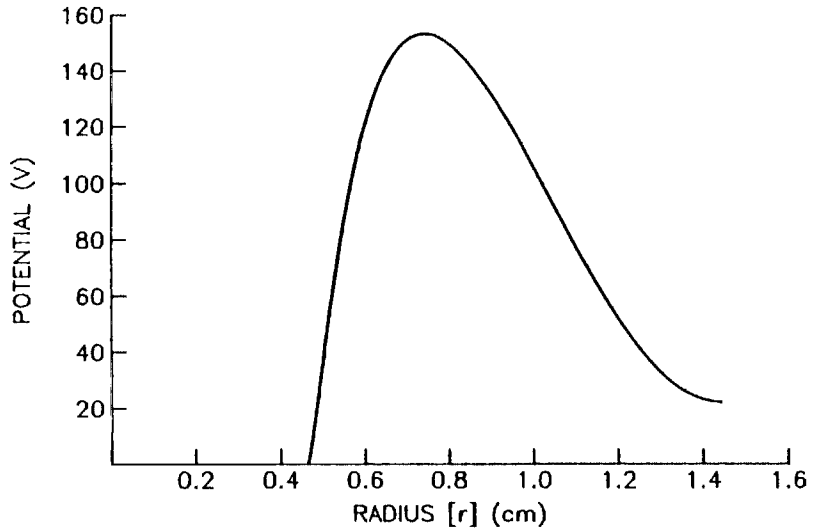

a. Potential Profile

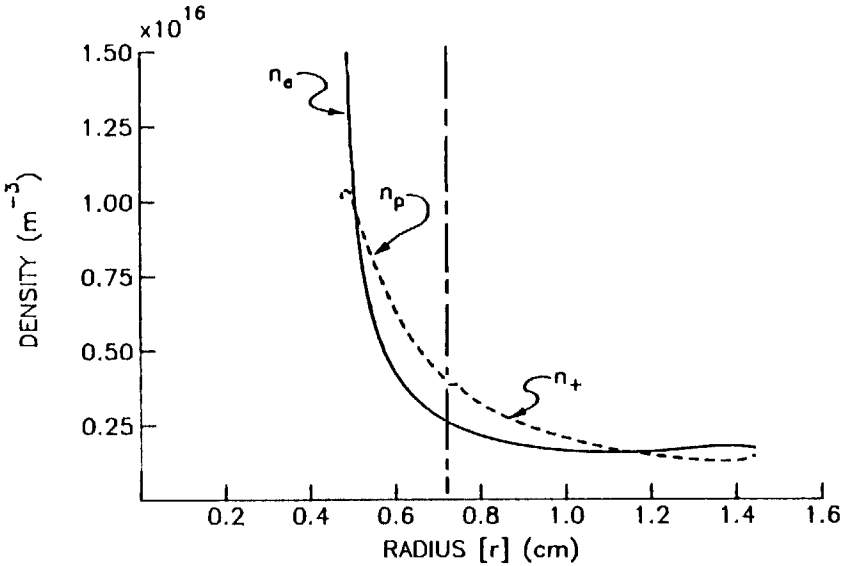

b. Charged Particle Densities

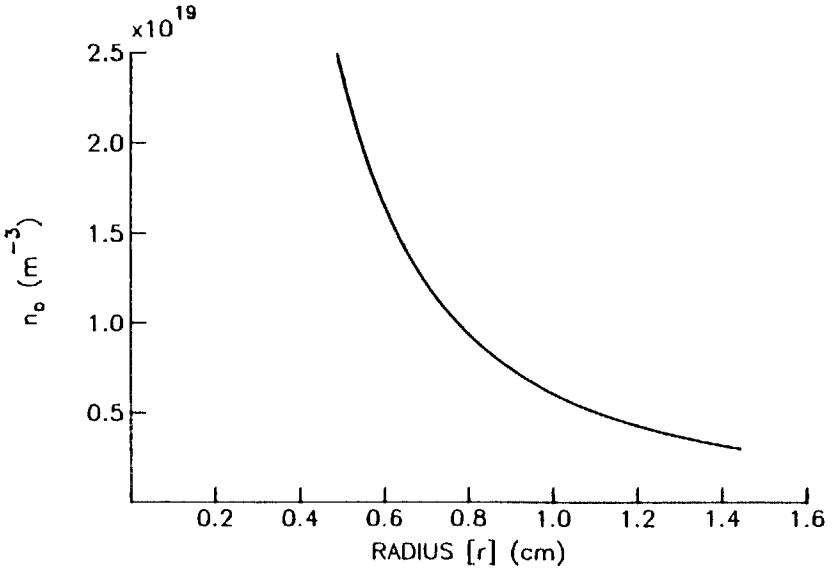

c. Neutral Density

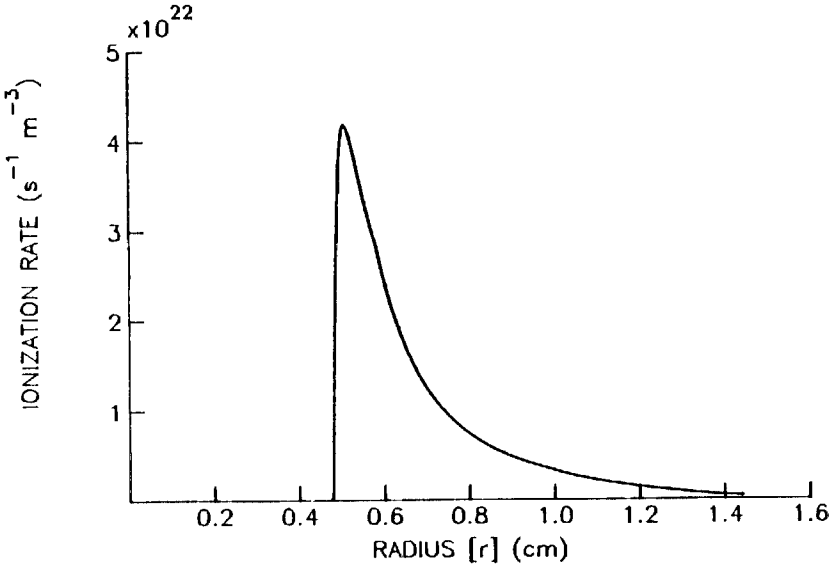

d. Ion Production Rate

Fig. 8 Typical Computed Electron Emission Results

5 and 11.5 mm as shown in Fig. 8b. The neutral atom density variation throughout the potential hill region is shown in Fig. 8c. When this information was combined with the data shown in Figs. 8a and 8b the ion production rate per unit volume was calculated and it is plotted in Fig. 8d. By integrating the volumetric ion production rate over the entire potential hill region volume, the total ion current flowing from this region was calculated to be 4.10 mA. An ion current of about 1.94 mA (J_+) was found to be flowing from the potential hill region to the downstream boundary and 2.16 mA (J_p) was found to be flowing to the electron source boundary. These ion creation rates (expressed as currents) are small compared to the emission current. This suggests that the assumptions made in deriving this model are probably valid and that very little power should be required from the streaming electrons to remove low energy electrons (resulting from inelastic collisions) from the potential hill as quickly as they are produced.

Comparison of Theory and Experiment

The procedures used to obtain the numerical results given in Table 1 and Fig. 8 were applied to obtain additional solutions over ranges of electron emission currents and flowrates. The effect of electron emission current and flowrate on the current density and maximum energy of ions flowing away from the hollow cathode discharge were also measured using the RPA described previously. The experimentally measured and theoretically predicted effect of emission current on these quantities are compared in Fig. 9 under conditions where the RPA was positioned 20 cm downstream of the contactor. Figure 9a shows the high energy ion current density increasing with electron emission current, at a smaller slope than the "theoretical" curve. The theoretical predictions of high energy ion current density were made by first finding the

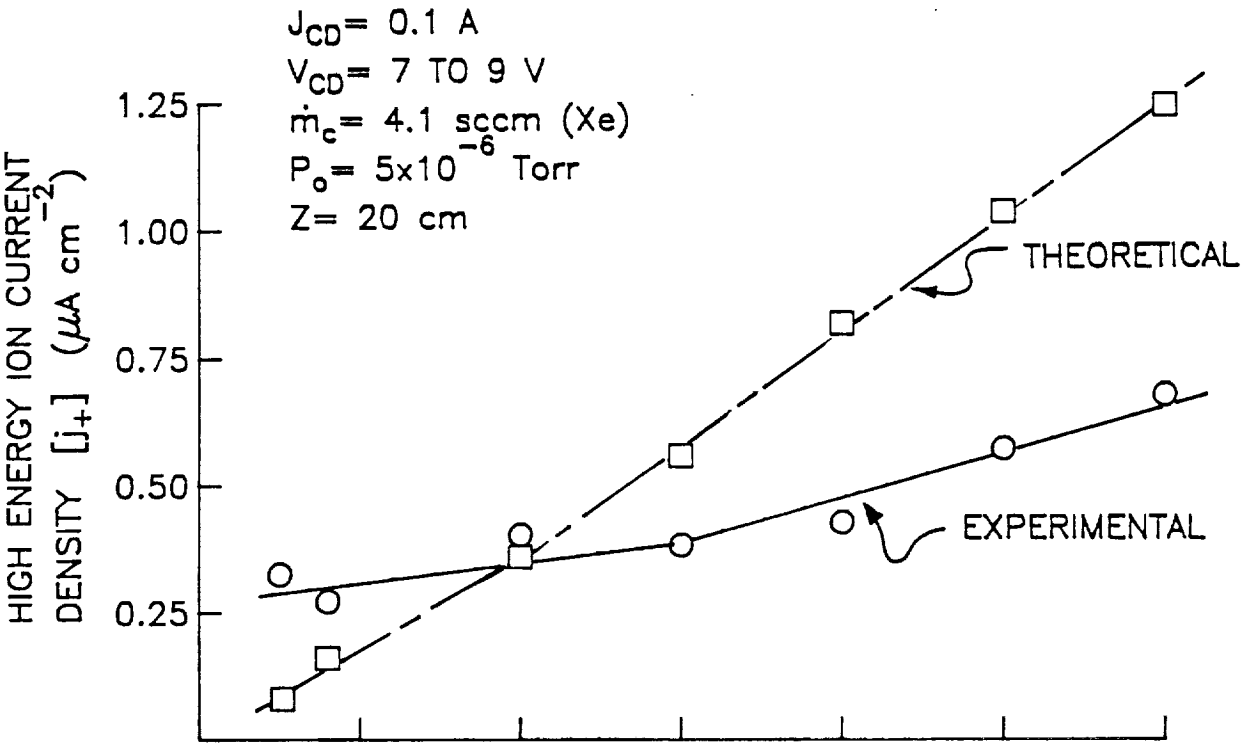

a. Ion Current Density

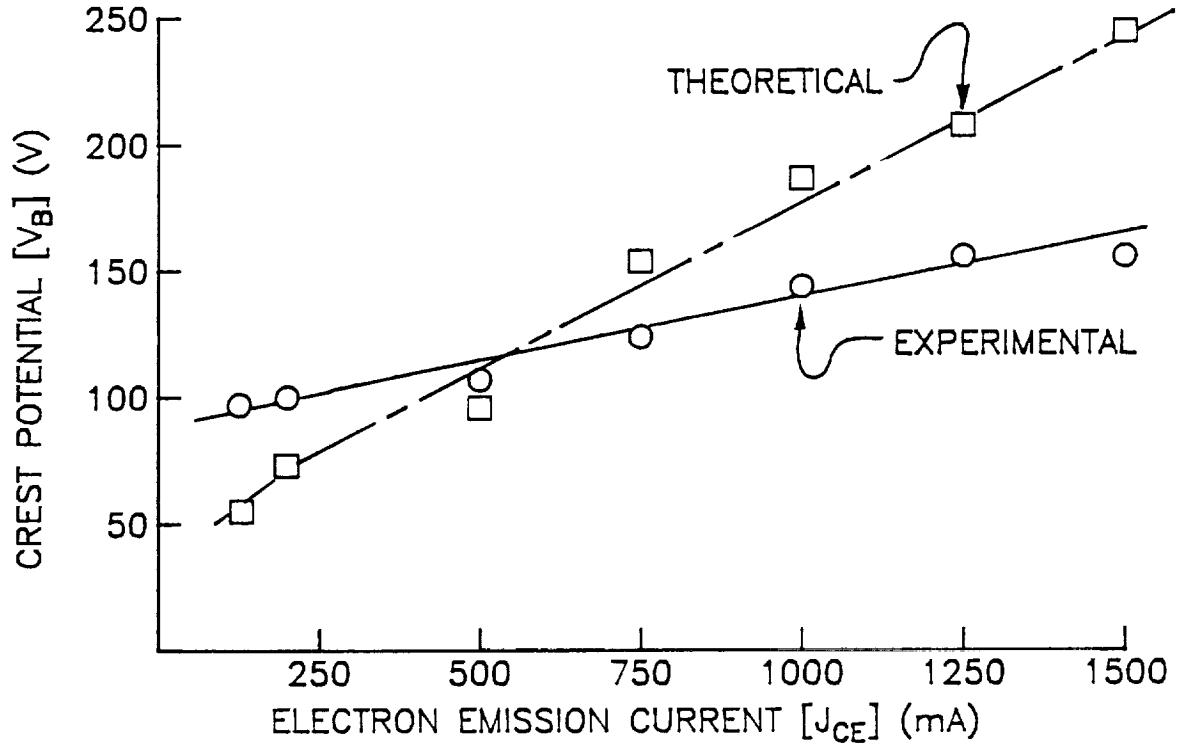

b. Crest Potential

Fig. 9 Computed Effects of Emission Current

ion current emitted from the potential hill region to the downstream boundary for the particular electron emission current as explained in the numerical example of Table 1 and Fig. 8. Next, this current was divided by the surface area at a radius of 20 cm (i.e. $\psi r^2 \approx 2\pi[20]^2$ cm^2 $\approx$ 2500 cm^2) to obtain the current density at this location. Although the two curves shown in Fig 9a do not coincide, the agreement between the experiment and numerical model is considered to be good considering the assumptions made in the model. Uncertainties in experimental conditions as well as in the ionization cross sections could easily cause the level of error indicated in Fig. 9a. It is noted that better agreement could be artificially generated in this simple one-dimensional model by adjusting the solid angle ψ with each electron emission current. However, it is felt that two-dimensional (or possibly three-dimensional) effects probably determine the subtle trends in the experimental data so attempts to adjust ψ to obtain better agreement would not be justified.

Figure 9b contains a comparison of experimentally and theoretically determined crest potentials. Again, relatively good agreement and a similar trend for the crest potential to increase with electron emission current for both curves is shown. The actual positions of r_e, r_B, and r_A at the electron emission levels corresponding to Fig. 9 are shown in Fig. 10. The most notable trend in this figure is that larger values of r_A correspond to smaller values of electron emission current. Together with Fig. 9b, this suggests that not only are crest potentials greater at higher electron emission currents, but electric field strengths are also higher.

The effect of contactor flowrate on the experimentally measured and theoretically predicted high energy ion current and crest potential are shown in Fig. 11. The theoretical predictions (triangular and solid circular data points) and experimental

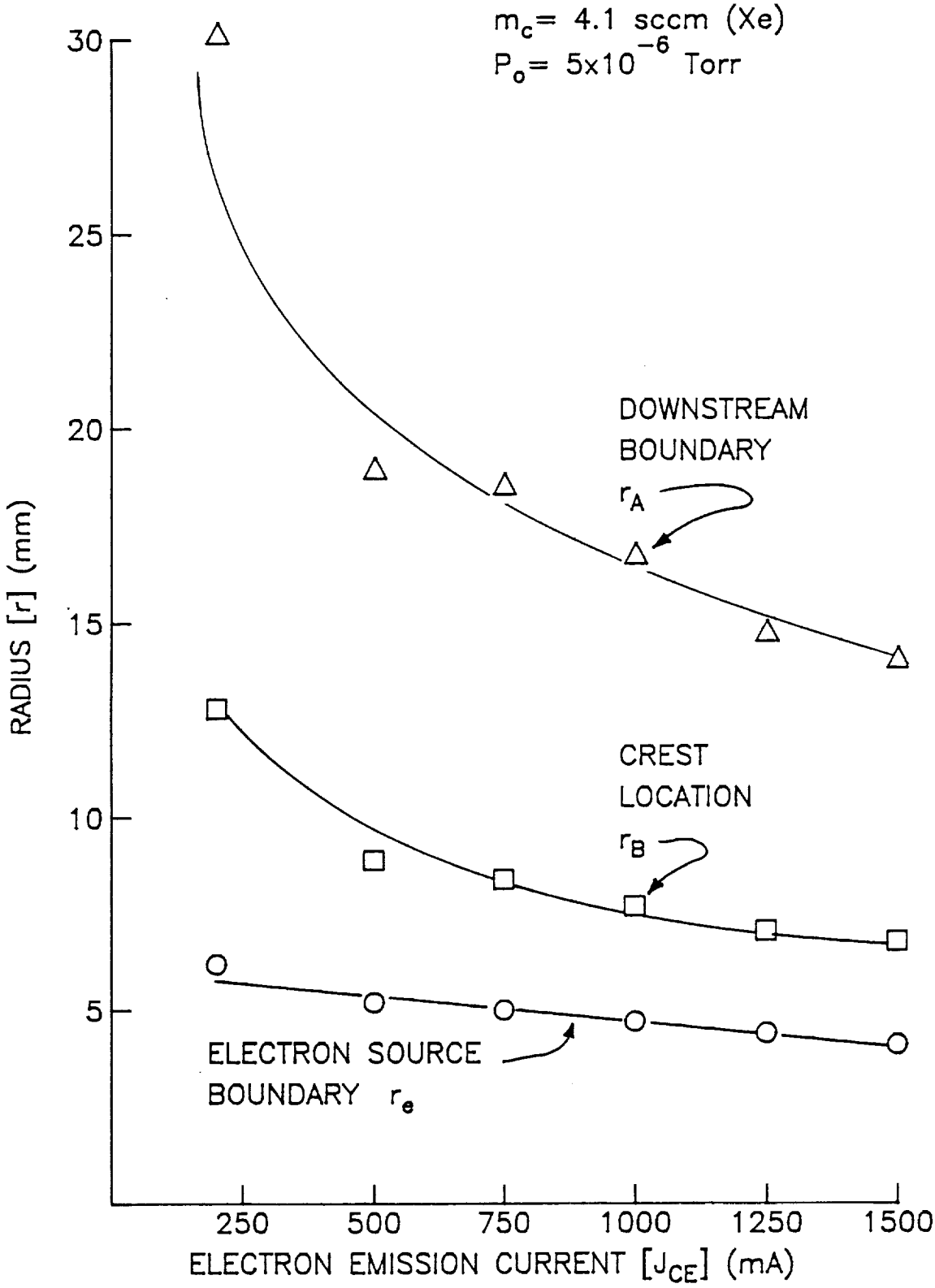

Fig. 10 Computed Values of Downstream, Crest, and Electron Source Boundaries as Functions of Electron Emission Current

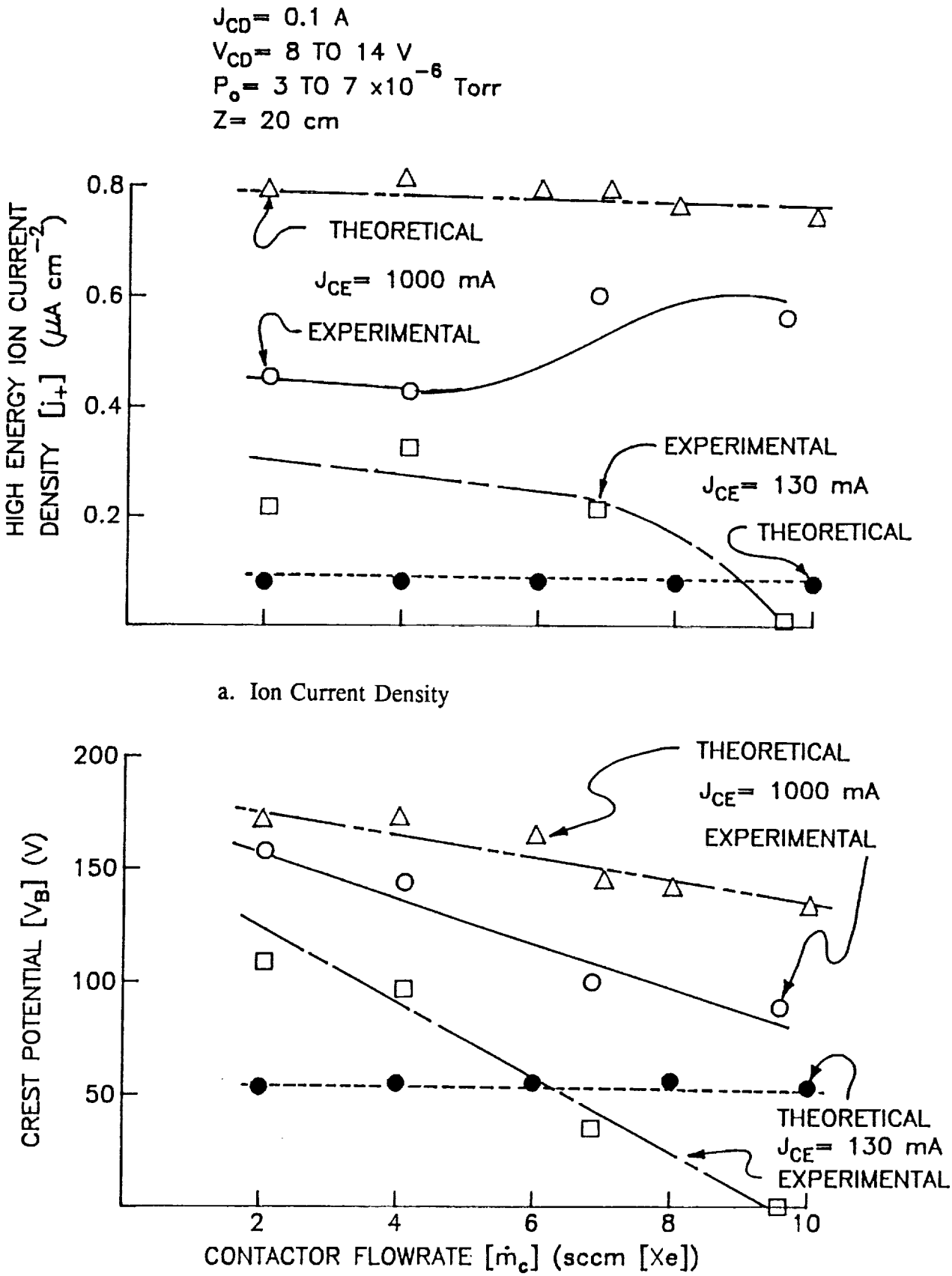

a. Ion Current Density

b. Crest Potential

Fig. 11 Computed Effects of Contactor Flowrate

measurements (circular and square data points) of high energy ion current density corresponding to the 130 and 1000 mA electron emission levels are shown to exhibit comparable magnitudes in Fig. 11a. The theoretical crest potential data for the 1000 mA condition shown in Fig. 11b also show good agreement with experiments, and the predicted and measured crest potentials show a similar trend (both decrease with flowrate). However, the predicted and measured crest potentials corresponding to the 130 mA condition do not show the same trends. Note that current density measurements made at an electron emission current of 130 mA (shown in Fig. 11a) indicate, at a contactor flowrate of 9.6 sccm, that no high energy ions are present. At this high flowrate and low electron emission level, apparently no potential hill structure is needed to assist electron emission from the high density plasma near the contactor hollow cathode. Numerical modelling of the 130 mA condition was difficult to perform at the higher flowrates and, in order to obtain a steady solution, the downstream potential V_A had to be artificially increased to ~ 14 V (from actual measured values of 8 to 12 V) to realize a convergent solution. This action probably caused the relatively constant value of crest potential (about 55 V as shown in Fig. 11b) to be exhibited at high flowrates. For the convenience of the reader, the predicted values of r_e, r_B, and r_A corresponding to Fig. 11 are shown in Fig. 12. It shows that higher flowrates induce larger radii and these values appear to grow linearly with flowrate.

The level of agreement between the model and experiment shown in Figs. 9 and 11 is considered to be good. In addition, the rate of ion production (expressed as a current) in the potential hill region is small compared to the electron emission current for all of the comparisons made in these figures. Hence, the rate of low energy

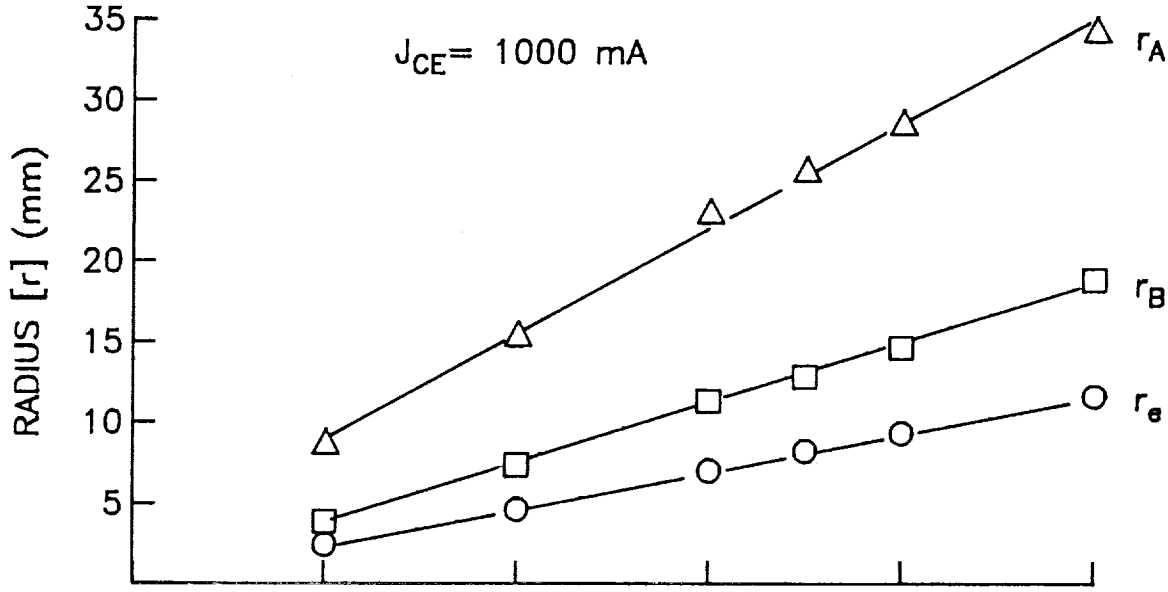

a. 1000 mA Emission Current Condition

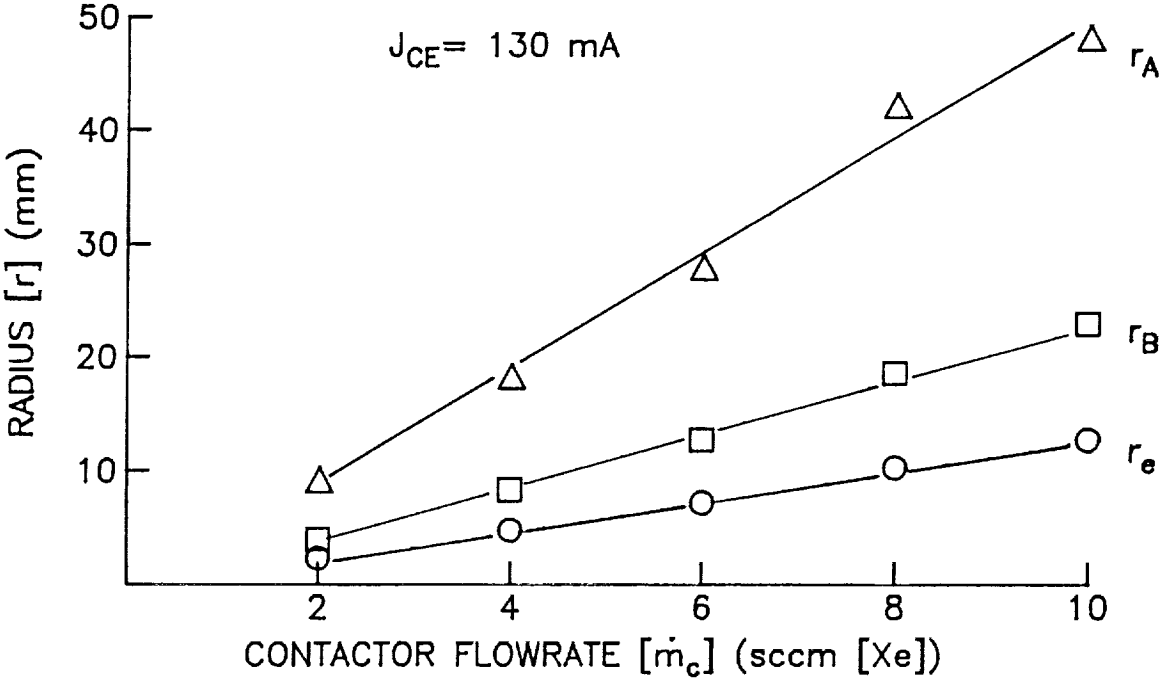

b. 130 mA Emission Current Condition

Fig. 12 Computed Values of Downstream, Crest and Electron Source Boundaries as Functions of Contactor Flowrate

(secondary) electron production is also small and it should be possible to remove them as they are produced using a small fraction of the power in the streaming electron beam. Recall their removal via an undefined mechanism is assumed in the model.

Conclusions

Experimental observations of a hollow cathode-based plasma contactor emitting electrons to a ambient plasma suggest that a potential hill structure develops close to the contactor cathode. It is postulated that the potential hill is created by a region of positive space charge, and ions produced in this region can gain substantial energies as they are accelerated away from the region. By measuring the energies of these ions, the height of the potential hill can be inferred. In general, an increase in contactor flowrate tends to reduce the potential at the crest of the hill, while larger emission current levels tend to increase it.

A simple model that reflects the effects of ionization, ion and electron acceleration and the space-charge induced by the ions and electrons describes the essential features derived from experimental observations of hollow cathodes emitting electrons. Specifically, it yields magnitudes of potential hill height and current density of ions flowing from the potential hill that agree with experimental results. Further, the predicted effects of electron emission current and contactor flowrate on these features agree with experimentally observed trends. It is noted that the total current of ions emitted to the expanding plasma is estimated to be small compared to the electron emission current (i.e. typically less than 0.2 %). This suggests that only a small fraction of the electrons flowing from the contactor to the expanding plasma interact with and possibly ionize neutral atoms while they stream through the potential hill region.

CSU AND CNR-IFSI BI-LATERAL EXPERIMENTS ON PLASMA CONTACTORS

Introduction

Experiments have been conducted independently at Colorado State University [1], NASA Lewis Research Center [3], and the Italian Institute of Interplanetary Space Physics [2,19] on the electron collection characteristics of hollow cathode-based plasma contactors. The most basic experiments involve biasing a plasma contactor and its associated plasma cloud (or high density plasma plume) positive with respect to an ambient plasma and measuring the current which is collected under this applied voltage. Typically, most of the voltage drop between the contactor (and its plasma cloud) and the ambient plasma develops across a double layer. Previous experiments conducted at CSU, NASA Lewis, and IFSI have detected double layers, but some differences have been noted. In order to address these differences, a bi-lateral research program was initiated between CSU and IFSI. This report, which describes work conducted under this program, presents the results of recent experiments conducted in the IFSI facility on the electron collection mode of the plasma contacting process. The goals of the IFSI experiments were to 1) investigate the effects of magnetic field on the electron collection process, 2) compare and calibrate Langmuir and emissive probe plasma diagnostic techniques, and 3) operate a hot filament cathode-based ion source as an ambient plasma generator.

Apparatus and Procedures

In order to study the electron collection process, the apparatus shown schematically in Figs. 13 and 14 was set up at IFSI. Physically this apparatus is

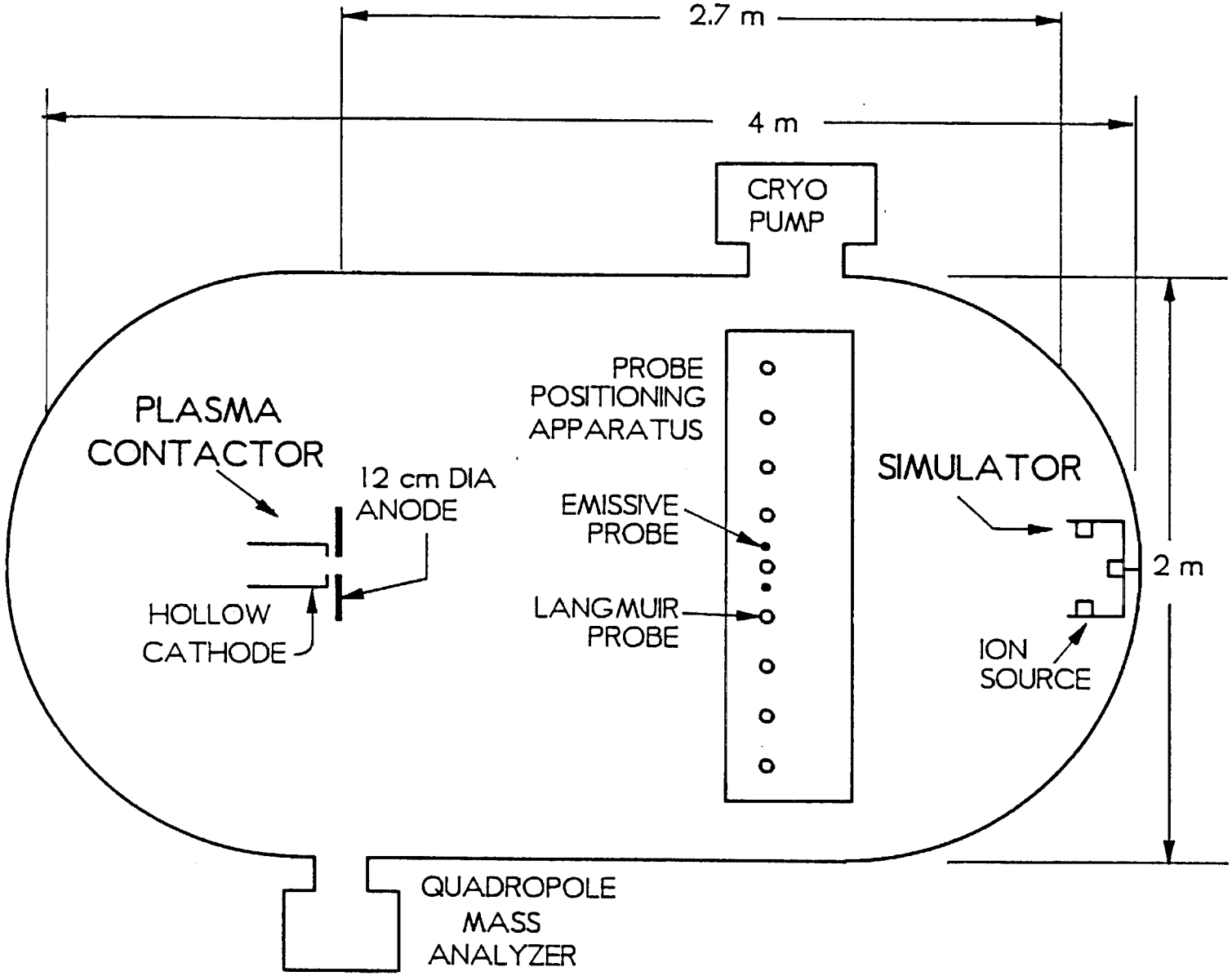

Fig. 13 IFSI Vacuum and Probing System Schematic

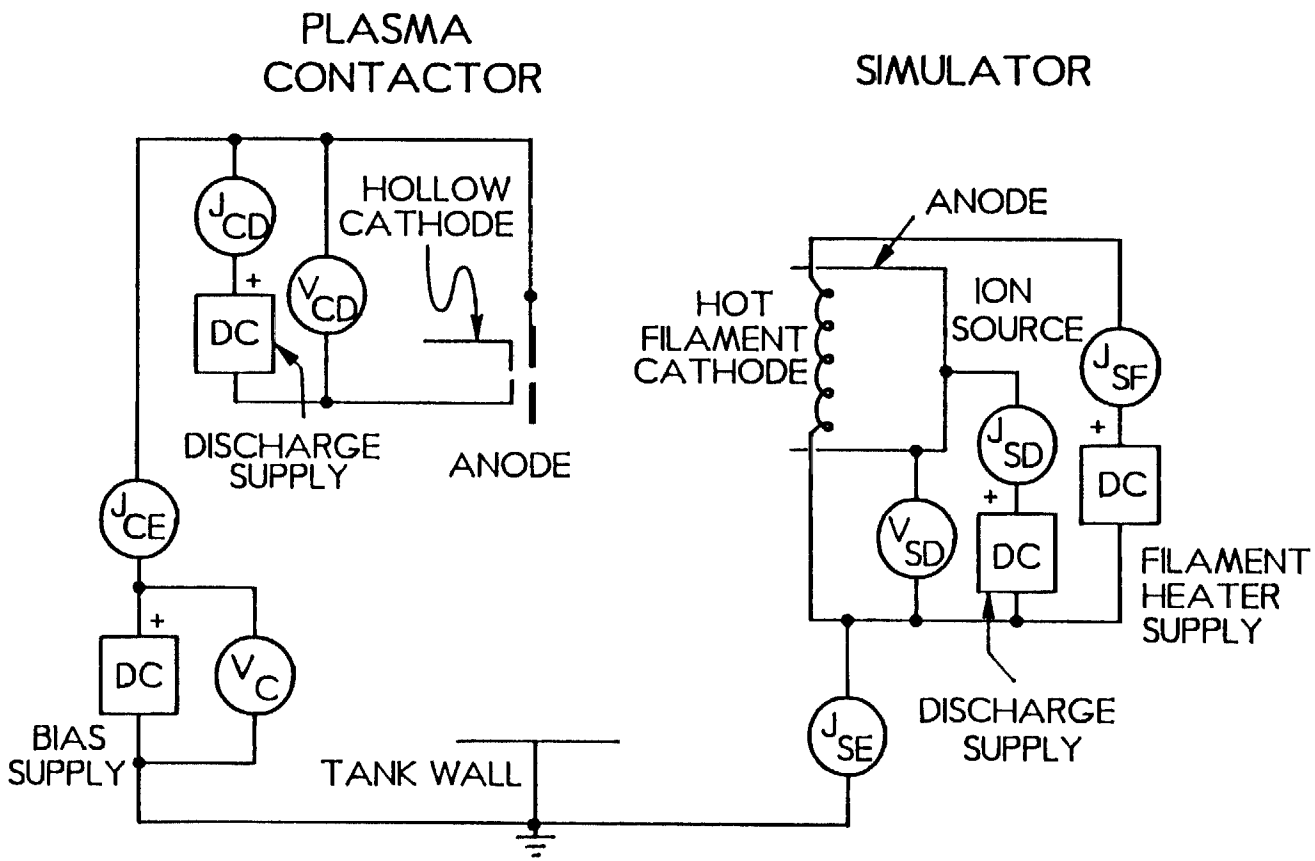

Fig. 14 IFSI Electrical Schematic

similar to the one described previously in this report. The simulator and contactor devices are separated by 2.7 m and are located within a 2 m dia. by 4 m long, stainless steel vacuum chamber. The contactor utilizes a 6.4 mm dia, orificed hollow cathode which houses an electron emitting Ta foil insert. The hollow cathode orifice is 0.38 mm in diameter and the contactor anode is a 12 cm dia. stainless steel plate with a 1 cm dia. tantalum insert that has a 5 mm dia. orifice in it. The anode plate and its tantalum insert are located concentric with the hollow cathode centerline at a plane ~ 2 mm downstream of the cathode orifice plate.

Typical tests were conducted by heating the contactor hollow cathode to a temperature where significant thermionic electron emission could occur from its insert (~ 1300 K), establishing an expellant (xenon) flowrate through it, and biasing its anode positive using the discharge supply to initiate a cathode-to-anode discharge. The simulator, a hot-filament equipped ion source shown in Fig. 15 and described in Ref. 12, was also started. Next, the desired contactor and simulator flowrates and discharge current levels were established; the contactor was biased relative to the simulator using the bias power supply; and voltage, current and probing instrument data were collected. The tests described in this attachment were performed at a contactor flowrate and discharge current of 1.2 sccm (Xe) and 0.6 A, respectively. This operating condition induced a 30 V discharge voltage, and a background pressure of 16×10^{-6} Torr. The simulator flowrate was about 2 sccm (Xe), and its discharge current and voltage were set to 0.6 A and 54 V, respectively.

The plasma environment produced between the contactor and the simulator was probed using the instruments shown in Fig. 13. The emissive probes were used to measure plasma potential and they were compared to Langmuir probe plasma potential

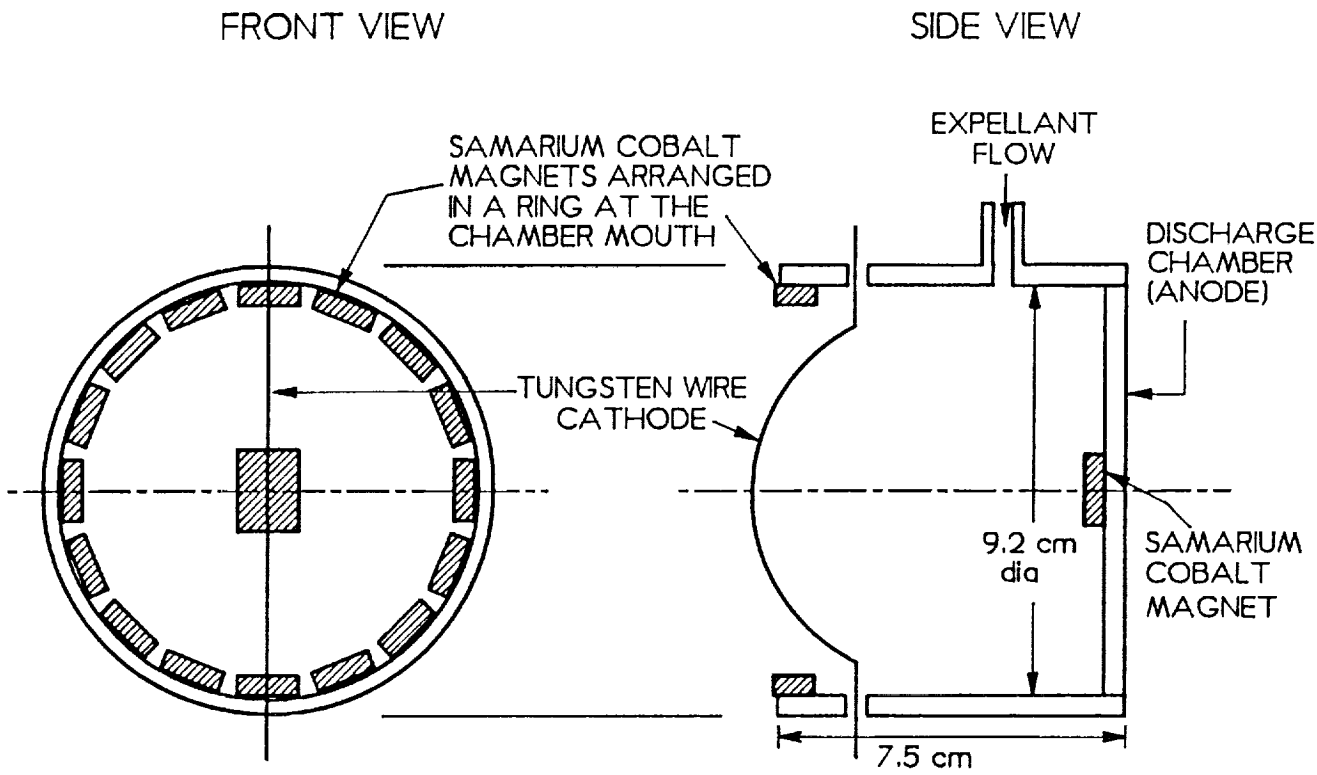

Fig. 15 Hot Filament Cathode-based Simulator

measurements. The nine Langmuir and two emissive probes were fixed to a movable platform that could position them on a line that intersected the centerline and was parallel to the plane of the contactor anode at axial positions varying from 1 to 265 cm (measured from the contactor anode). Figure 16 is a perspective view of the probes showing their locations in relation to the plasma contactor. The center Langmuir probe was positioned directly in front of the plasma contactor orifice, and the two emissive probes were positioned 3 cm from the axis on each side. The nine Langmuir probes were equally spaced at intervals of 12 cm.

The magnetic field present in the region between the contactor and simulator could be controlled in both magnitude and direction by large Helmholtz coils which encircled the stainless steel vacuum tank. In order to study its effect on the electron collection process, various magnetic field configurations were imposed. They included 1) a zero magnetic field, the geo-magnetic field was nulled; 2) axial fields, those directed along the axis joining the contactor and simulator; and 3) transverse fields, those aligned perpendicular to the axis joining the contactor and simulator.

Results and Discussion

Figures 17 and 18 show typical plasma property data that were either measured directly or computed from measurements made in the IFSI laboratory. Figure 17 corresponds to a condition where the Earth's magnetic field was nulled and 100 mA of electrons were being collected by the contactor from the ambient plasma. The emissive probe data in the upper plot of Fig. 17 show the potential variation through the double layer that develops between the contactor plasma cloud and the ambient plasma. It reveals a double layer across which a 27 V potential difference develops in the region between Z = 15 and 30 cm. Two energy distribution function

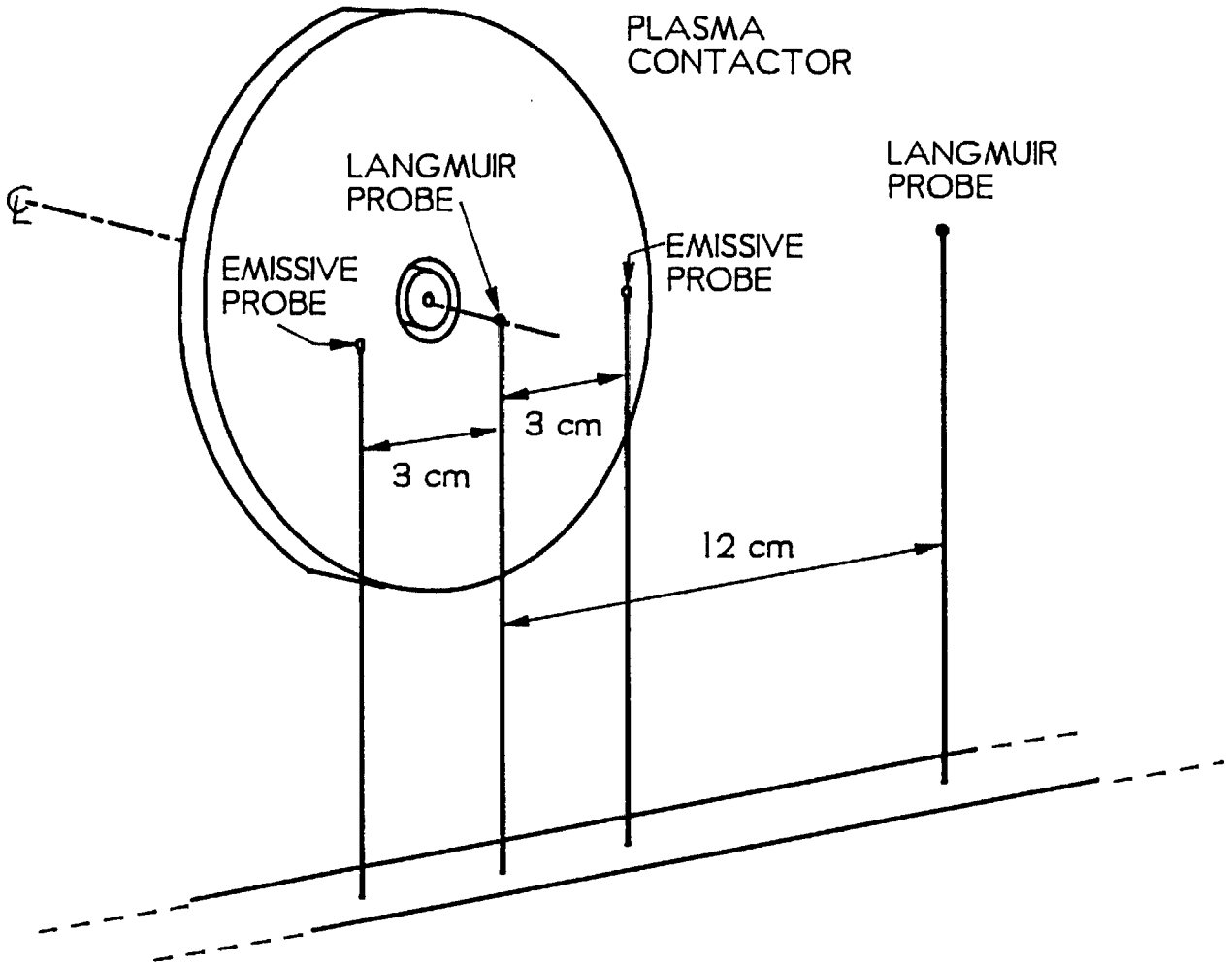

Fig. 16 Emissive and Langmuir Probe Arrangement

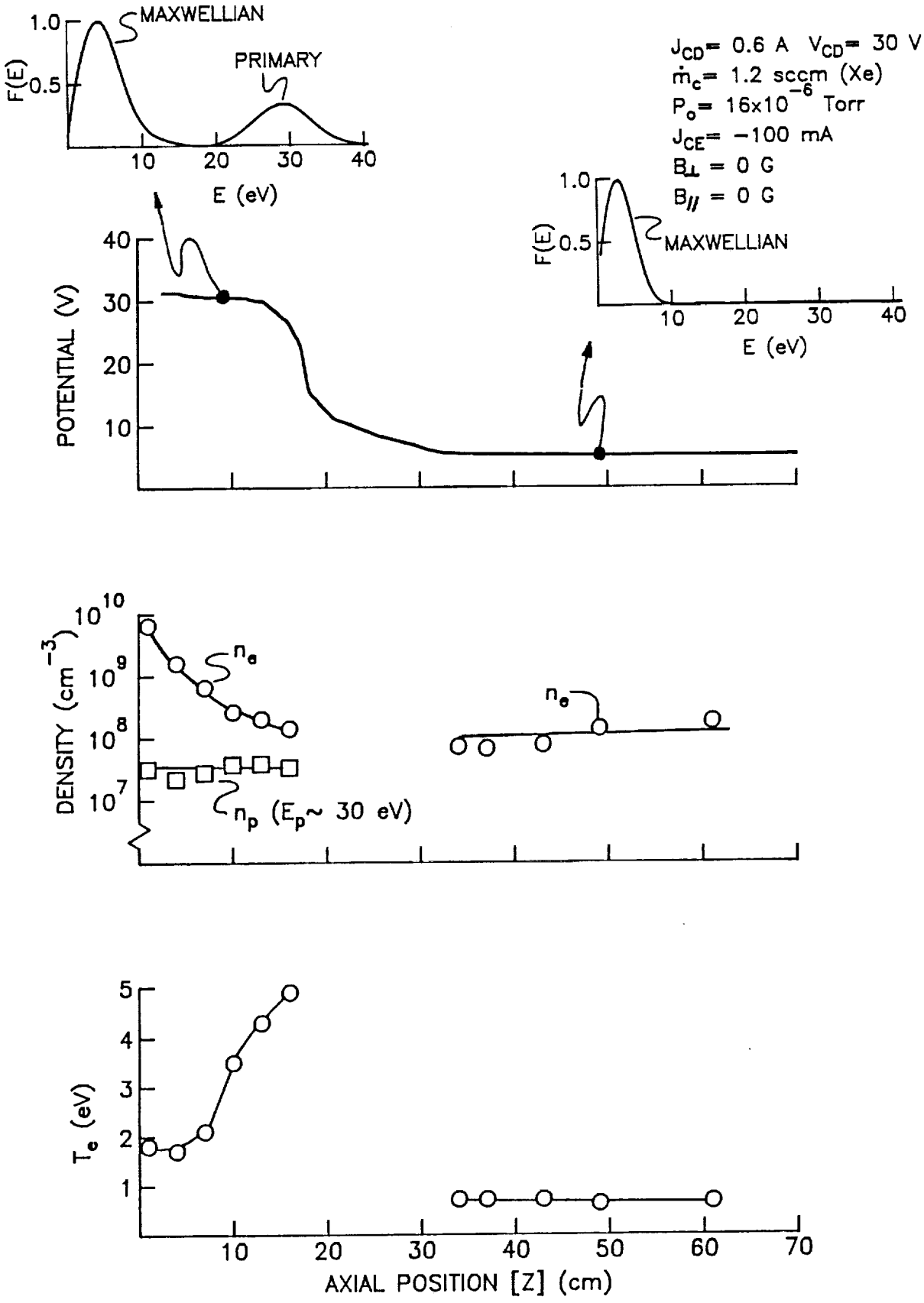

Fig. 17 Typical Axial Plasma Property Profiles (Nulled Magnetic Field)

plots derived from Langmuir probe data that describe the electrons at axial positions on either side of the double layer (10 and 49 cm) are shown adjacent to the plasma potential profile. The downstream distribution function (at 49 cm) suggests that only one group of electrons is present in the ambient plasma and they appear to be Maxwellian. On the other hand, the upstream distribution function (at 10 cm) shows a high energy group in addition to the Maxwellian one. It is believed that electrons accelerated from the ambient plasma through the double layer and into the upstream contactor plasma cloud region, are the ones that induce the non-thermal (high energy) hump centered near 30 eV.

The middle and bottom plots in Fig. 17 contain electron density and electron temperature data obtained from Langmuir probe measurements made in the contactor plasma cloud and ambient plasma regions. The Maxwellian electron group density is shown to be quite high near the contactor and to decrease rapidly with increasing axial position. The primary electron density is lower and it remains relatively constant within the contactor plasma cloud. It is noted that the densities of the Maxwellian and primary electrons in the contactor plasma cloud were calculated using the CSU Langmuir probe analysis program, which is based on the assumption that two electron groups are present in the plasma. One group is modelled as Maxwellian, while the other one (the primary group) is assumed isotropic and mono-energetic. The program solves for the Maxwellian group temperature and density and the primary group energy and density by using a non-linear, least-squares curve-fit to the portion of the Langmuir probe data in the electron retarding region. The properties of the electrons were also analyzed using a computer program developed by U. Guidoni, et. al. at IFSI. Although two separate Maxwellian groups can be used in the IFSI program to model

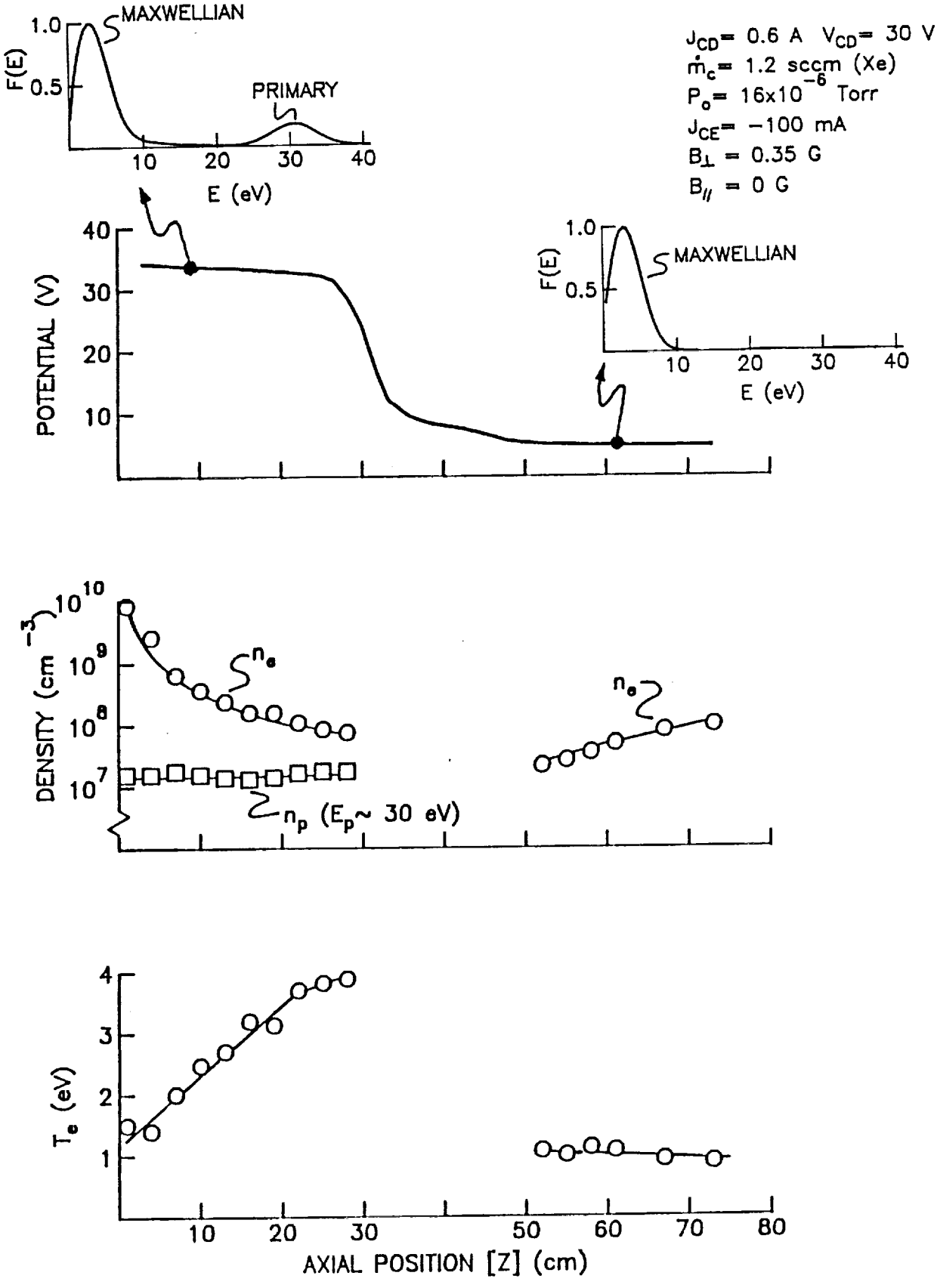

Fig. 18 Typical Axial Plasma Property Profiles (0.35 G Transverse Magnetic Field)

the plasma, the program was used to analyze only the colder Maxwellian electron groups in the contactor plasma cloud and ambient plasmas. Results obtained using these two analysis techniques will be compared shortly.

The data in the middle plot of Fig. 17 show the Maxwellian electron density in the ambient plasma region remains relatively constant with axial position. Temperatures computed from Langmuir probe measurements for the Maxwellian electron groups in the ambient plasma and contactor cloud regions are shown in the lowest plot. It reveals a very low electron temperature in the ambient plasma (about 0.7 eV) and an electron temperature that rises in the contactor cloud from 1.8 eV close to the contactor to 5 eV at a position near the double layer. This rise in electron temperature is consistent with observations made in other double layer tests [14]. It suggests electron heating is occurring near the double-layer boundary possibly as a result of turbulent interactions between the high energy and Maxwellian electrons present in the contactor plasma cloud. Indications of higher electron temperatures could also be due to an error in the Langmuir probe analysis program that becomes significant when the high energy electron signal begins to dominate the colder electron group signal at locations close to the double layer boundary.

Figure 18 contains data which correspond to a transverse magnetic field with a magnitude of 0.35 G. It is organized similar to Fig. 17 and it shows many of the trends attributed to Fig. 17. However, one important difference between Figs. 17 and 18 is the position of the double layer. It is located further downstream of the contactor (between 26 and 35 cm) when the transverse field is applied. Presently, the processes which cause the contactor cloud to enlarge in the axial direction when a transverse field is applied are not understood.

Extensive Langmuir probe data were collected at IFSI (about 1500 traces!) for several electron collection currents and magnetic field configurations. A comparison of the results obtained using both the IFSI and CSU analysis programs for Langmuir probe traces taken on the centerline is included in Tables 2 and 3. These tables also include emissive probe measurements of plasma potential ($V_{P,EP}$), which are typically used in the CSU analysis routine but not in the IFSI one. These plasma potential data are seen to agree with values obtained from Langmuir probe measurements found using the IFSI program ($V_{P,LP}$). It is noted, however, that a significant difference tends to develop between plasma potentials determined from the Langmuir and emissive probe measurements at small values of electron collection current--see the top data set of Table 2, for example. This error is believed to be caused by the fact that the emissive and Langmuir probes do not measure potential at the same location (they are separated by 3 cm). When the electron collection current is large, the plasma contactor cloud is also large and both probes tend to lie within it when they are close to the contactor. At low emission currents, however, the emissive probe may lie outside of what tends to be a small contactor plasma cloud. It is also noted that it is probably impossible to interpret Langmuir probe data taken within and very near the double-layer region. It is because of this that the data of Figs. 17 and 18 and Tables 2 and 3 do not show electron densities and temperatures/energies in this region.

In general, the agreement between the IFSI and CSU Langmuir probe data analysis programs is considered to be good. The largest differences are observed between Maxwellian temperature results in the contactor plasma cloud region. A contributor to this difference was the large voltage step (1 V) used in the acquisition of the Langmuir probe data. As mentioned previously, another difficulty encountered

Table 2 Centerline Plasma Property Comparisons for Nulled Magnetic Field

J_{CE} = -50 mA
$B_{\perp}$ = 0 G
$B_{//}$ = 0 G

				<- CSU ANALYSIS ->				<- IFSI ANALYSIS ->	
Ref. #	**Z**	**$V_{P,EP}$**	**$V_{P,LP}$**	**n_e**	**T_e**	**n_p**	**E_p**	**n_e**	**T_e**
	(cm)	(V)	(V)	(cm^{-3})	(eV)	(cm^{-3})	(eV)	(cm^{-3})	(eV)
rb001	1	9.0	12.6	$1.1x10^{10}$	1.3	$6.0x10^{6}$	14	$7.4x10^{9}$	1.6
rb004	4	9.0	11.6	$1.9x10^{9}$	1.6	—	—	$1.3x10^{9}$	1.4
rb007	7	8.4	10.1	$8.2x10^{8}$	1.3	$1.4x10^{7}$	9.4	$4.7x10^{8}$	1.8
vb010	10	7.7	10.8	$1.2x10^{9}$	1.3	$1.4x10^{7}$	11	$2.5x10^{8}$	2.4
vb031	31	4.0	3.9	$1.1x10^{8}$	0.60	—	—	$1.0x10^{8}$	0.50
vb037	37	4.0	4.3	$1.4x10^{8}$	0.52	—	—	$9.6x10^{7}$	0.68
vb043	43	4.0	4.3	$1.4x10^{8}$	0.55	—	—	$8.7x10^{7}$	0.70
vb055	55	4.0	3.9	$1.4x10^{8}$	0.55	—	—	$9.9x10^{7}$	0.68

J_{CE} = -100 mA
$B_{\perp}$ = 0 G
$B_{//}$ = 0 G

				<- CSU ANALYSIS ->				<- IFSI ANALYSIS ->	
Ref. #	**Z**	**$V_{P,EP}$**	**$V_{P,LP}$**	**n_e**	**T_e**	**n_p**	**E_p**	**n_e**	**T_e**
rc001	1	31	35	$6.5x10^{9}$	1.8	$3.2x10^{7}$	33	$6.5x10^{9}$	1.9
rc004	4	31	33	$1.6x10^{9}$	1.7	$2.2x10^{7}$	32	$1.3x10^{9}$	2.2
rc007	7	31	34	$6.5x10^{8}$	2.1	$2.8x10^{7}$	32	$4.3x10^{8}$	3.7
vc010	10	30	35	$2.6x10^{8}$	3.5	$3.8x10^{7}$	34	$2.4x10^{8}$	6.8
vc013	13	30	36	$2.0x10^{8}$	4.3	$3.9x10^{7}$	35	$1.9x10^{8}$	8.7
vc016	16	26	34	$1.4x10^{8}$	4.9	$3.4x10^{7}$	33	$1.5x10^{8}$	9.2
vc034	34	5.2	5.5	$7.2x10^{7}$	0.72	—	—	$7.6x10^{7}$	0.86
vc037	37	5.1	5.5	$6.7x10^{7}$	0.72	—	—	$9.5x10^{7}$	0.96
vc043	43	5.1	5.5	$7.7x10^{7}$	0.72	—	—	$6.9x10^{7}$	0.96
vc049	49	5.1	5.5	$1.4x10^{8}$	0.64	—	—	$7.4x10^{7}$	0.91
vc061	61	5.1	5.5	$1.8x10^{8}$	0.68	—	—	$8.6x10^{7}$	0.89

J_{CE} = -150 mA
$B_{\perp}$ = 0 G
$B_{//}$ = 0 G

				<- CSU ANALYSIS ->				<- IFSI ANALYSIS ->	
Ref. #	**Z**	**$V_{P,EP}$**	**$V_{P,LP}$**	**n_e**	**T_e**	**n_p**	**E_p**	**n_e**	**T_e**
vd004	4	45	46	$8.9x10^{8}$	2.1	$2.6x10^{7}$	43	$6.3x10^{8}$	3.3
vd007	7	45	46	$6.1x10^{8}$	1.8	$2.9x10^{7}$	43	$2.7x10^{8}$	4.6
vd010	10	44	46	$3.1x10^{8}$	2.2	$3.0x10^{7}$	43	$2.0x10^{8}$	5.6
vd013	13	44	46	$1.8x10^{8}$	3.0	$3.8x10^{7}$	44	$1.6x10^{8}$	8.6
vd016	16	44	47	$1.8x10^{8}$	2.7	$2.7x10^{7}$	45	$1.4x10^{8}$	7.5
vd019	19	42	45	$1.0x10^{8}$	4.0	$3.5x10^{7}$	43	$9.9x10^{7}$	12.6
vd040	40	6.0	6.2	$1.1x10^{8}$	0.95	—	—	$5.6x10^{7}$	1.2
vd043	43	5.8	6.2	$1.0x10^{8}$	0.95	—	—	$6.3x10^{7}$	1.1
vd046	46	5.8	6.3	$7.9x10^{7}$	1.1	—	—	$6.4x10^{7}$	1.2
vd049	49	5.8	6.3	$7.6x10^{7}$	1.1	—	—	$6.5x10^{7}$	1.2
vd055	55	5.8	6.3	$8.4x10^{7}$	1.0	—	—	$6.8x10^{7}$	1.1
vd061	61	5.8	6.3	$8.9x10^{7}$	1.0	—	—	$6.9x10^{7}$	1.1

Table 3 Centerline Plasma Property Comparisons (Zero, Transverse, and Axial Magnetic Fields)

J_{CE} = -100 mA
$B_\perp$ = 0 G
$B_{//}$ = 0 G

| <——— CSU ANALYSIS ———> | <- IFSI ANALYSIS -> |

Ref. #	Z	$V_{P,EP}$	$V_{P,LP}$	n_e	T_e	n_p	E_p	n_e	T_e
	(cm)	(V)	(V)	(cm^{-3})	(eV)	(cm^{-3})	(eV)	(cm^{-3})	(eV)
rc001	1	31	35	$6.5x10^9$	1.8	$3.2x10^7$	33	$6.5x10^9$	1.9
rc004	4	31	33	$1.6x10^9$	1.7	$2.2x10^7$	32	$1.3x10^9$	2.2
rc007	7	31	34	$6.5x10^8$	2.1	$2.8x10^7$	32	$4.3x10^8$	3.7
vc013	13	30	36	$2.0x10^8$	4.3	$3.9x10^7$	35	$1.9x10^8$	8.7
vc016	16	26	34	$1.4x10^8$	4.9	$3.4x10^7$	33	$1.5x10^8$	9.2
vc034	34	5.2	5.5	$7.2x10^7$	0.72	—	—	$7.6x10^7$	0.86
vc037	37	5.1	5.5	$6.7x10^7$	0.72	—	—	$9.5x10^7$	0.96
vc049	49	5.1	5.5	$1.4x10^8$	0.64	—	—	$7.4x10^7$	0.91
vc061	61	5.1	5.5	$1.8x10^8$	0.68	—	—	$8.6x10^7$	0.89

J_{CE} = -100 mA
$B_\perp$ = 0.35 G
$B_{//}$ = 0 G

| <——— CSU ANALYSIS ———> | <- IFSI ANALYSIS -> |

Ref. #	Z	$V_{P,EP}$	$V_{P,LP}$	n_e	T_e	n_p	E_p	n_e	T_e
re001	1	33	36	$8.4x10^9$	1.5	$1.6x10^7$	36	$6.0x10^9$	1.7
re004	4	34	36	$2.6x10^9$	1.4	$1.6x10^7$	35	$1.2x10^9$	2.1
ve007	7	34	37	$6.5x10^8$	2.0	$1.8x10^7$	35	$4.8x10^8$	3.0
ve013	13	33	37	$2.4x10^8$	2.7	$1.4x10^7$	35	$1.7x10^8$	4.8
ve019	19	33	37	$1.6x10^8$	3.1	$1.5x10^7$	35	$1.2x10^8$	6.1
ve025	25	32	37	$8.6x10^7$	3.8	$1.8X10^7$	36	$7.0x10^7$	9.6
ve046	46	6.0	5.5	$4.9x10^7$	0.99	—	—	$2.0x10^7$	1.3
ve052	52	4.8	5.1	$2.9x10^7$	1.0	—	—	$2.1x10^7$	1.1
ve058	58	4.7	5.6	$6.7x10^8$	0.95	—	—	$3.6x10^7$	1.1
ve061	61	4.6	5.5	$1.2x10^8$	0.82	—	—	$5.0x10^7$	1.1

J_{CE} = -100 mA
$B_\perp$ = 0 G
$B_{//}$ = 0.35 G

| <——— CSU ANALYSIS ———> | <- IFSI ANALYSIS -> |

Ref. #	Z	$V_{P,EP}$	$V_{P,LP}$	n_e	T_e	n_p	E_p	n_e	T_e
rk001	1	33	33	$5.2x10^9$	1.4	$2.1x10^7$	31	$3.2x10^9$	1.8
vk004	4	34	33	$8.8x10^8$	1.8	$1.3x10^7$	31	$6.0x10^8$	2.5
vk007	7	34	33	$3.4x10^8$	1.9	$1.7x10^7$	32	$2.5x10^8$	3.5
vk013	13	34	34	$3.4x10^8$	2.4	$2.9x10^7$	33	$1.6x10^8$	5.9
vk016	16	30	34	$2.7x10^8$	2.5	$4.1x10^7$	34	$1.3x10^8$	9.5
vk034	34	5.0	6.0	$4.6x10^7$	1.7	—	—	$5.7x10^7$	1.2
vk037	37	4.9	6.0	$8.8x10^7$	1.5	—	—	$6.3x10^7$	1.2
vk040	40	4.8	5.9	$1.1x10^8$	1.3	—	—	$6.5x10^7$	1.2
vk043	43	4.8	5.9	$1.1x10^8$	1.3	—	—	$6.7x10^7$	1.2

when attempting to evaluate the properties of the colder electron group present in the contactor plasma cloud was the perturbation and masking of this signal by the high energy electron group signal.

The data of Table 2 were measured when the magnetic field strength in the region between the contactor and simulator was reduced to zero. The plasma property measurements that yielded these data were made along the tank centerline at electron collection currents of 50, 100, and 150 mA. Table 3 contains data obtained at an electron collection current of 100 mA in magnetic field environments of zero, 0.35 G transverse, and 0.35 G axial. The data associated with the zero and 0.35 G axial fields are very similar, but the 0.35 G transverse field causes the contactor plasma clouds to extend further downstream as shown in Fig. 18.

The effects of magnetic field on the contactor plasma cloud and double layer regions at 1 G axial and transverse conditions can be seen by comparing the data of Figs. 19 and 20. Figure 19 shows the contactor plasma cloud extends further downstream and the double layer voltage drop increases from zero to 55 V as the electron collection current is increased from 50 to 200 mA in a 1 G axial field environment. This observation is in agreement with the unpublished results of previous electron collection experiments conducted at CSU and LeRC when low contactor flowrates were used and no ignited mode transition was observed. Results similar to those shown in Fig. 19 were also obtained when the magnetic field was set to zero.

Figure 20 shows plasma potential profiles obtained at a 1 G transverse magnetic field condition. The profile corresponding to 50 mA of electron collection displays one double layer. However, as the electron collection current is increased to 100 and 150 mA, two double layers develop. In addition to multiple double layers

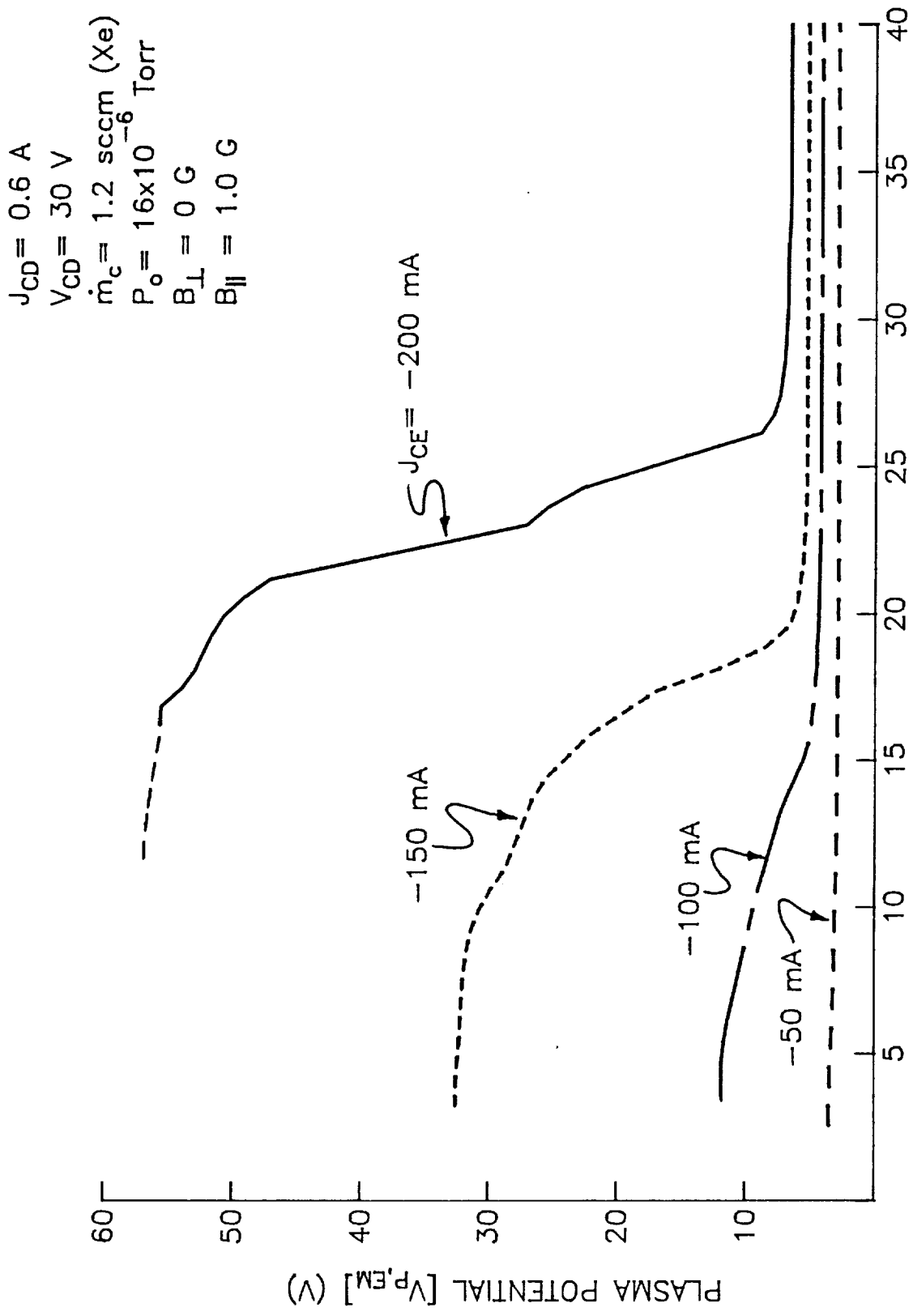

Fig. 19 Effect of Electron Collection Current on Plasma Potential Profiles in a 1.0 G Axial Magnetic Field

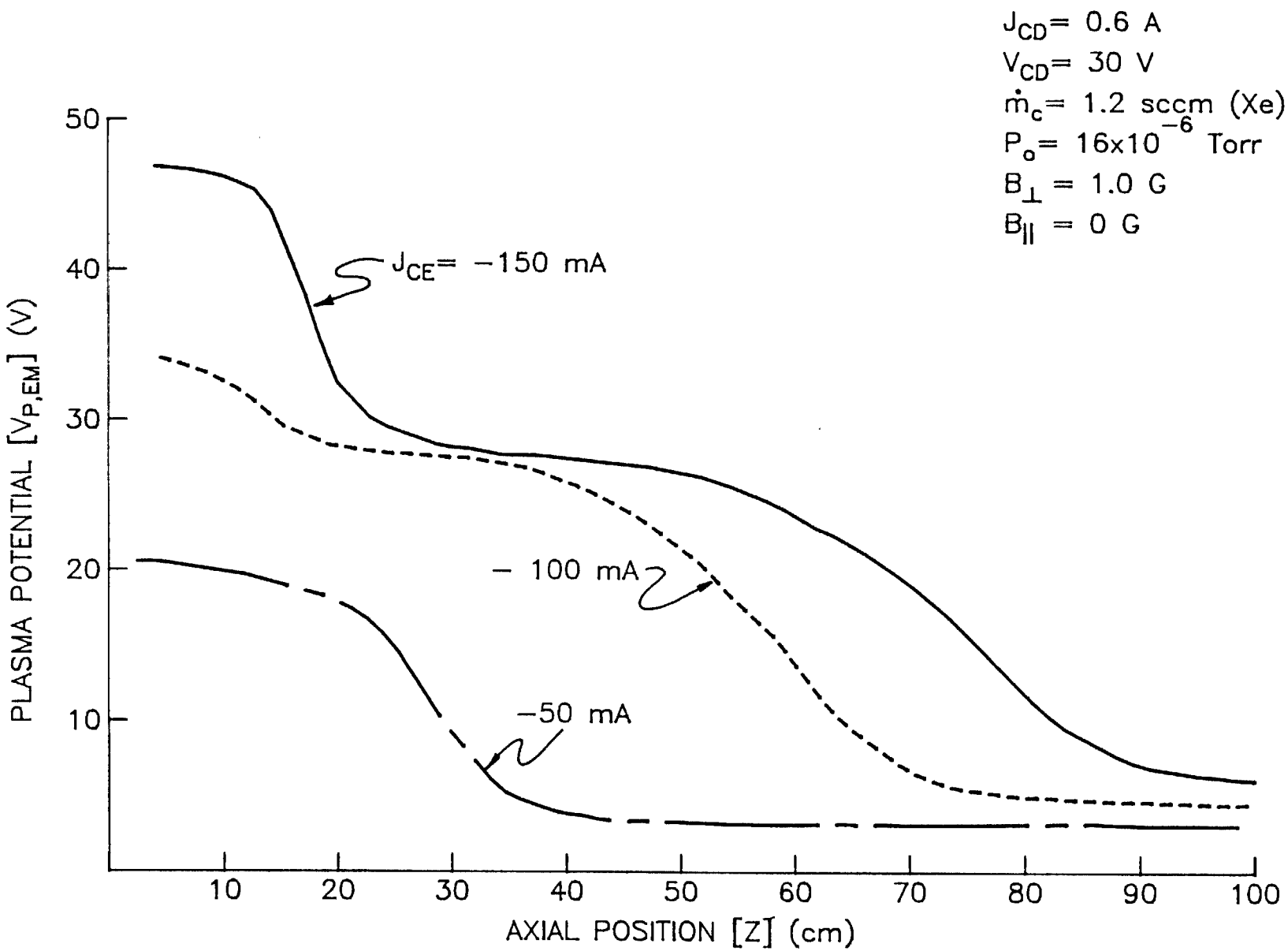

Fig. 20 Effect of Electron Collection Current on Plasma Potential Profiles in a 1.0 G Transverse Magnetic Field

occurring at higher electron collection currents, higher plasma noise was observed. Unfortunately, the noise data were qualitative and numerical comparisons cannot be made. The noise level tended to be greatest through the multiple double layer regions and much lower close to the contactor and in the ambient plasma region.

Up to this point, emphasis has been placed on the axial variation of plasma properties. The uniformity of the ambient plasma properties in the radial direction are shown in Fig. 21. This figure contains plasma potential, density and temperature data at the nulled, 0.35 G transverse, and 0.35 G axial magnetic field conditions at fixed axial positions of 61, 61, and 43 cm, respectively. The plasma potential is shown to be relatively constant at about 6 V over the 1 m radial region investigated, although it increases to about 8 V at a radial position of -50. It is noted that the negative radial positions correspond to locations between the centerline and the cryo-pump side of the facility (see Fig. 13) and positive radial positions correspond to locations between the centerline and the quadropole mass analyzer. Both negative and positive radial position data were shown in Fig. 21 in order to display the level of symmetry in the ambient plasma. The middle plot in Fig. 21 contains plasma density data, which show maximum densities on the centerline. Although the plasma density data show some scatter, the density is generally highest for the axial magnetic field condition and lowest for the transverse magnetic field. The electron temperature is nearly constant in the radial direction at about 1.2 eV as shown in the bottom plot of Fig. 21.

The maximum magnetic field that could be induced in the IFSI facility was 1.6 G, and plasma potential profiles corresponding to a transverse field of this magnitude are shown in Fig. 22. The low electron collection current of 50 mA shows a single well-defined double layer which develops between 35 and 45 cm. At higher currents of

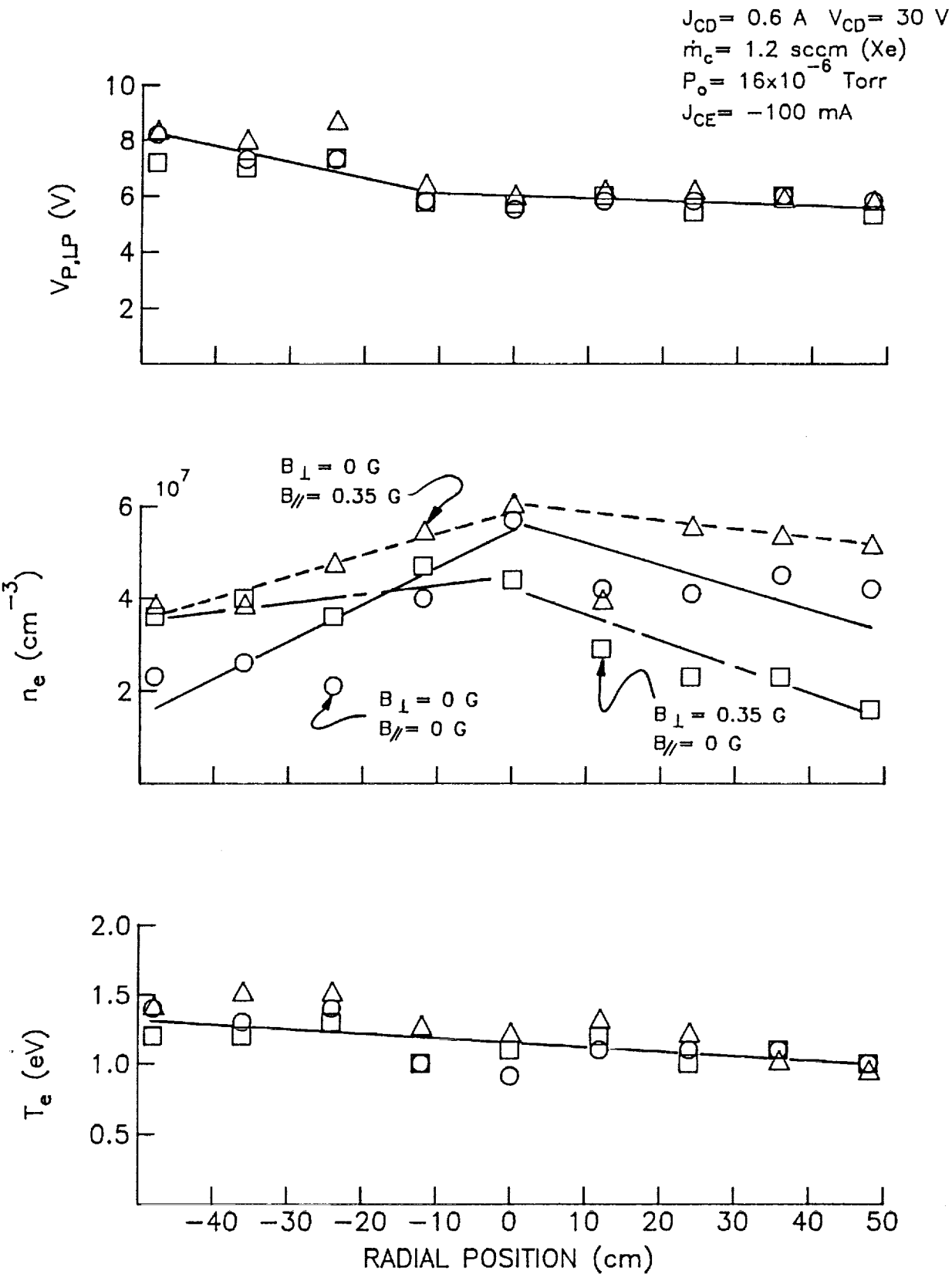

Fig. 21 Radial Plasma Property Profiles in the Ambient Plasma

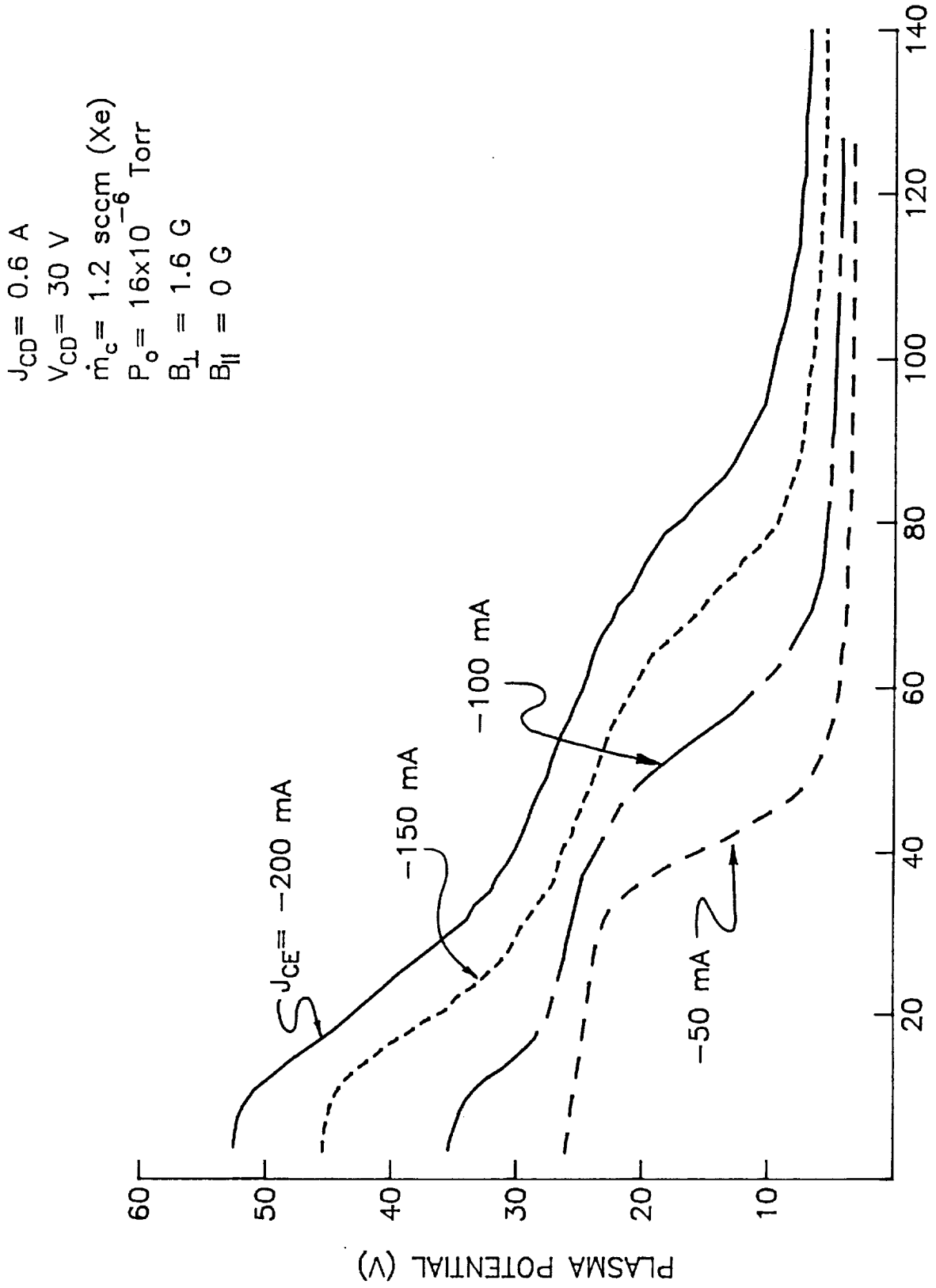

Fig. 22 Effect of Electron Collection Current on Plasma Potential Profiles in a Strong 1.6 G Transverse Magnetic Field

100, 150, and 200 mA, two double layers are shown to develop which are less well-defined and extend further downstream. In addition, as the current is increased, the total voltage drop across the double layer increases.

Conclusions

Similar double layers exhibiting large voltage drops and very distinct boundaries are observed in electron collection experiments conducted in both the IFSI and CSU laboratories. Independent plasma potential measurements made using Langmuir and emissive probes in regions away from the double layer agree well (typically within 1 V). However, emissive probes are attractive because they yield potential data that vary continuously through the double layer while Langmuir probes yield reliable plasma potential data only on either side of the double layer. Further, emissive probe results facilitate interpretation of the Langmuir probe data. A comparison of CSU and IFSI Langmuir probe analysis procedures suggest that both have advantages and disadvantages. The CSU analysis procedure can be used to model high energy, non-thermal electrons that are frequently present in the contactor plasma cloud. The IFSI procedure is easier to use when nearly-Maxwellian plasmas are being investigated and plasma potentials are being determined from thick-sheath Langmuir probe traces.

The effects of magnetic field strength (0 to 1.6 G) are small when the field is oriented along the direction of current flow between the contactor and simulator. Increases in the strength of a magnetic field oriented transverse to the current flow direction induce multiple double-layers and increased noise levels near the double layers.

ACKNOWLEDGEMENT

The efforts of Dr. Giuliano Vannaroni and Mr. Rizzierio Giovi of IFSI to make the CSU-IFSI bi-lateral program successful are gratefully acknowledged.

References

1. Williams, J.D., and P.J. Wilbur, "Ground-based Tests of Hollow Cathode Plasma Contactors," AIAA 89-1558-CP, Third Int'l Conf. on Tethers in Space, San Fransico, May 17-19, 1989, pp. 77-87.

2. Vannaroni, G., et. al., "Experimental Characterization of Hollow-Cathode Plasma Sources at Frascati," appears in "Space Tethers for Science in the Space Station Era," L.Guerriero and I.Bekey, eds., Societa Italiana Di Fisica, V.14, Venice, Italy, Oct. 4-8 1987, pp. 254-260.

3. Patterson, M.J., and R.S. Aadland, "Ground-based Plasma Contactor Characterization," appears in "Space Tethers for Science in the Space Station Era," L. Guerriero and I. Bekey, eds., Societa Italiana Di Fisica, V.14, Venice, Italy, Oct.4-8, 1987, pp. 261-268.

4. Gerver, M.J., D.E. Hastings, and M. Oberhardt, "Theory and Experimental Review of Plasma Contactors," Third Int'l Conf. on Tethers in Space, Additional Conference Presentations, San Fransico, May 17-19, 1989, pp. 49-95.

5. Katz, I. and V.A. Davis, "A Van der Waals-Like Theory of Plasma Double Layers," Phys. Fluids, V. B1, Oct. 1989, pp. 2121-2125.

6. Davis, V., I. Katz, M. Mandell, and D. Parks, "A Model of Electron Collecting Plasma Contactors," accepted by J. of Spacecraft and Rockets, preview paper dated Oct. 3, 1989.

7. Friedly, V.J. and P.J. Wilbur, "High Current Hollow Cathode Phenomena," AIAA paper 90-2587, July 18-20, 1990.

8. Siegfried, D.E., and P.J. Wilbur, "A Model for Mercury Orificed Hollow Cathodes: Theory and Experiment," AIAA Journal, V. 22, 1984, pp. 1405-1412.

9. Davis, W.D., and H.C. Miller, "Analysis of Electrode Products Emitted by dc Arcs in a Vacuum Ambient," J. Appl. Phys., V. 40, No. 3, April 1969, pp. 2212-2221.

10. Tanberg, R., "On the Cathode of an Arc Drawn in Vacuum," Physical Review, V. 35, May 1930, pp. 1080-1089.

11. Brophy, J.R. and P.J. Wilbur, "An Experimental Investigation of Cusped Magnetic Field Discharge Chambers," Int'l Electric Propulsion Conference, IEPC 84-70, Tokyo, Japan, 1984.

12. Williams, J.D. "Plasma Contactor Research," P.J. Wilbur, ed., NASA CR-185212, Feb. 1990.

13. Aston, G., and P.J. Wilbur, "Ion Extraction from a Plasma," J. Appl. Phys., V. 52, No. 4, 1981, pp. 2614-2626.

14. Herskowitz, N., "Review of Recent Laboratory Double Layer Experiments," Space Science Reviews, V. 41, 1985, pp. 351-391.

15. Anderson, J.R., "A Fourier Series Technique for Differentiating Experimental Data," Appendix C in NASA CR-182254, P.J. Wilbur, ed., Feb. 1989, pp.67-79. See also Lanczos, C., Applied Analysis, Prentice Hall Inc., Englewood Cliffs, New Jersey, 1964, pp. 219-221.

16. Rapp, D. and Englander-Golden, P., "Total Cross Sections for Ionization and Attachment in Gases by Electron Impact. I. Positive Ionization," J. of Chem. Phys., V. 34, No. 5, 1965, pp. 1464-1479.

17. Vannaroni G., et. al., "Data Analysis of Hollow Cathode Experiment to Support Electrodynamic Tether Applications", Istituto D. Fisica Dello Spazio Interplanetario, IFSI-89-16, Frascati, Italy, Sept. 1989.

18. Swift, J.D., and M.J.R. Schwar, Electrical Probes for Plasma Diagnostics, Elsevier Press, New York, 1970, p. 76.

19. CRC Handbook of Chemistry and Physics, R.C. Weast, Ed., 68th Edition, CRC Press Inc., Boca Raton, Florida, 1987, p. E395.

Appendix A

SIMPLE TECHNIQUE FOR OBTAINING ELECTRON ENERGY DISTRIBUTIONS

Introduction

In order to estimate the electron energy distribution function directly in a relatively low density, isotropic plasma using a spherical Langmuir probe, it is necessary to compute the second derivative of its current/voltage characteristic curve. It is generally very difficult to differentiate experimental data twice without amplifying the inherent noise in it to the point where it dominates any useful information. However, when clean, smooth experimental data are obtained using a device with a very low-pass filter and averaging capabilities like those available on Keithley 617 or 237 programmable electrometers and special numerical procedures are performed, realistic electron energy distributions can be generated. This appendix presents information about a very simple numerical method, which can yield convergent, relatively smooth derivatives of experimental data.

Application Example and Numerical Approach

A Langmuir probe trace typically consists of many discrete current/voltage data pairs [V_n, $J(V_n)$ -- n = 1, 2, ... , N] (equally-spaced in voltage). Figure A1 shows two typical, thick-sheath Langmuir probe traces constructed from plotting discrete current/voltage data sets. The probe voltage for these traces is referenced to the tank ground of the CSU facility, and they were measured in the contactor plasma cloud and ambient plasmas during a test in which a 50 mA electron current was being collected by the contactor from the ambient plasma. The trace obtained in the contactor plasma cloud contains features which suggest that a low-energy group (probably Maxwellian)

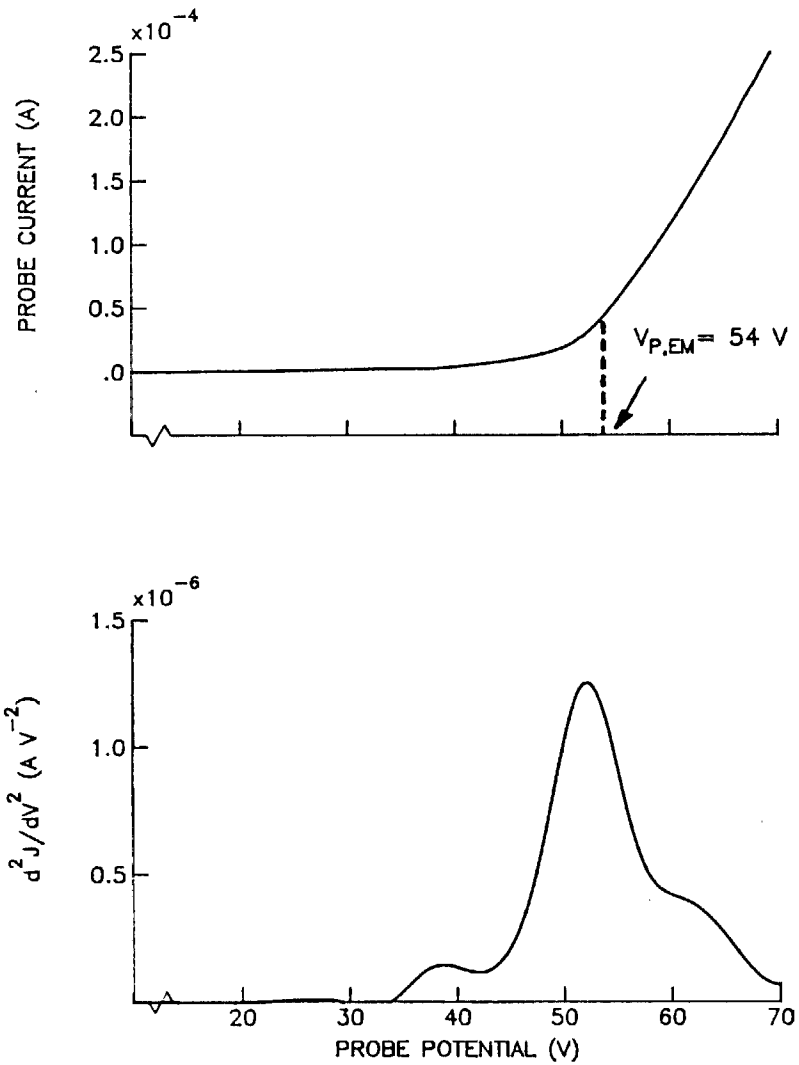

a. Contactor Plasma Cloud Data

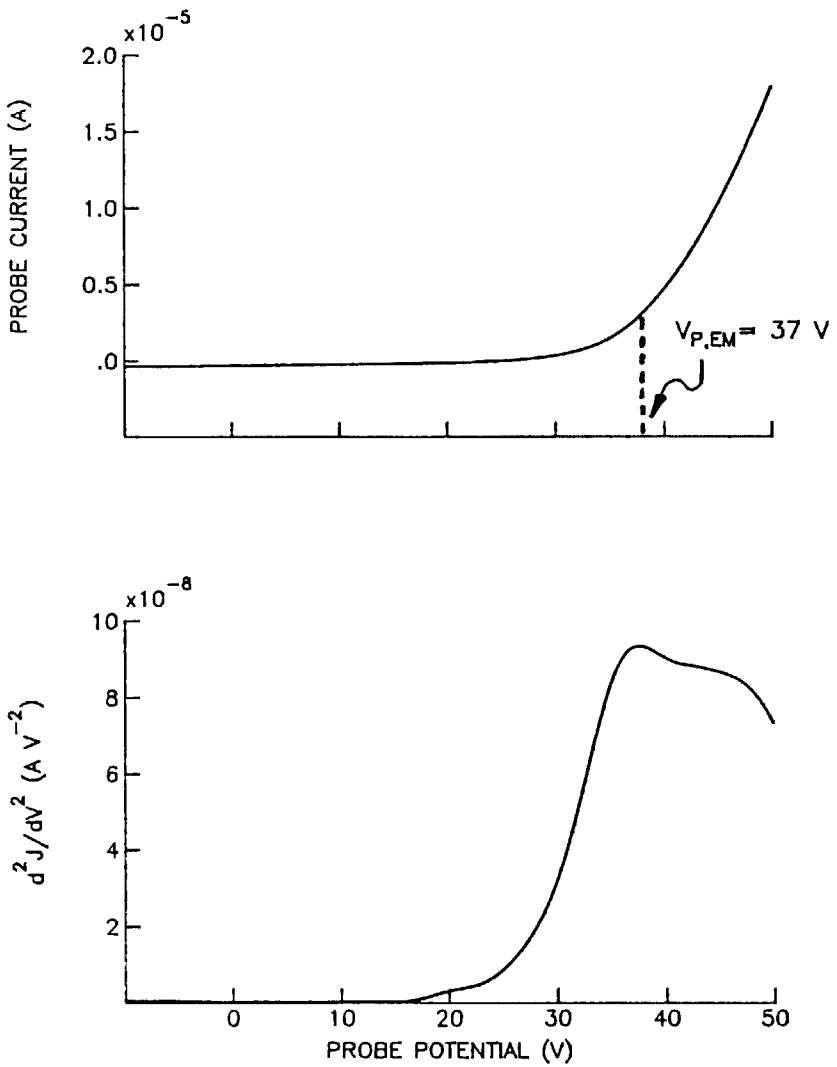

b. Ambient Plasma Data

Fig. A1 Typical Langmuir Probe Current/Voltage Traces Measured in the Ambient and Contactor Plasma Cloud Regions and Corresponding Second Derivatives

and a higher energy group of electrons are present, while the trace corresponding to the ambient plasma appears to contain only one, low-energy group. These characteristics can be seen more clearly by examining the second derivative curves shown beneath the current voltage traces. The second derivative curves can be used along with plasma potential measured by an emissive probe to compute the electron energy distribution function [18] using the equation

$$F(E) = \frac{2^{3/2} m_e^{1/2}}{e^{3/2} A_p} \sqrt{E} \frac{d^2 J}{dV^2} \quad . \text{(A1)}$$

In Eq. (A1), E is defined as the difference between plasma potential and any given probe potential (V).

In order to obtain the second derivative required in Eq. (A1), the discrete data points in a Langmuir probe trace were modified using the following procedure. First, a straight line, which connects the two end points of the trace, was subtracted from the data set:

In Eq. A2, x and y represent potential and modified current, respectively. The x and y data pairs are next represented as a continuous function (a Fourier sine series which was found using a least-squares fit)

i.e.

$$y \approx \sum_{j=1}^{m} A_j \sin\left[\frac{2\pi j x}{V_N - V_1}\right] \quad . \text{(A3)}$$

The number of terms in the series (m) was chosen to be half of the number of points in the data set (N) in order to avoid aliasing. Finally, the coefficients of the sine series were multiplied by the following convergence factor given by Lanczos [15]

$$B_j = \left[A_j \frac{\sin(\frac{j\pi}{N})}{\frac{j\pi}{N}} \right]^2 \quad . \quad \text{(A4)}$$

The new sine series composed of the B_j coefficients can be differentiated analytically. Finally, the overall procedure can be repeated to obtain the second derivative required in Eq. (A1).

Figure A2 contains two electron energy distribution functions which correspond to the Langmuir probe traces shown in Fig. A1 that were normalized to their most probable value. When the Langmuir probe traces were analyzed using traditional techniques, they exhibited a temperature of about 3 to 4 eV for the low-energy (Maxwellian) electron groups. However, the most probable energy of both distributions is about 3.5 eV and this value is higher than expected (if the low-energy group electrons were Maxwellian, this result suggests that their temperature would be about 2 * 3.5 eV = 7 eV). Another measure of a distribution is its full-width, half-maximum (FWHM) value. The distributions shown in Fig. A2 display FWHM values of 7 to 8 eV which correspond to Maxwellian distribution temperatures of 3.9 to 4.5 eV (i.e. $T_e \sim$ FWHM/1.8). This result agrees rather well with the Langmuir probe analysis estimates of 3 and 4 eV.

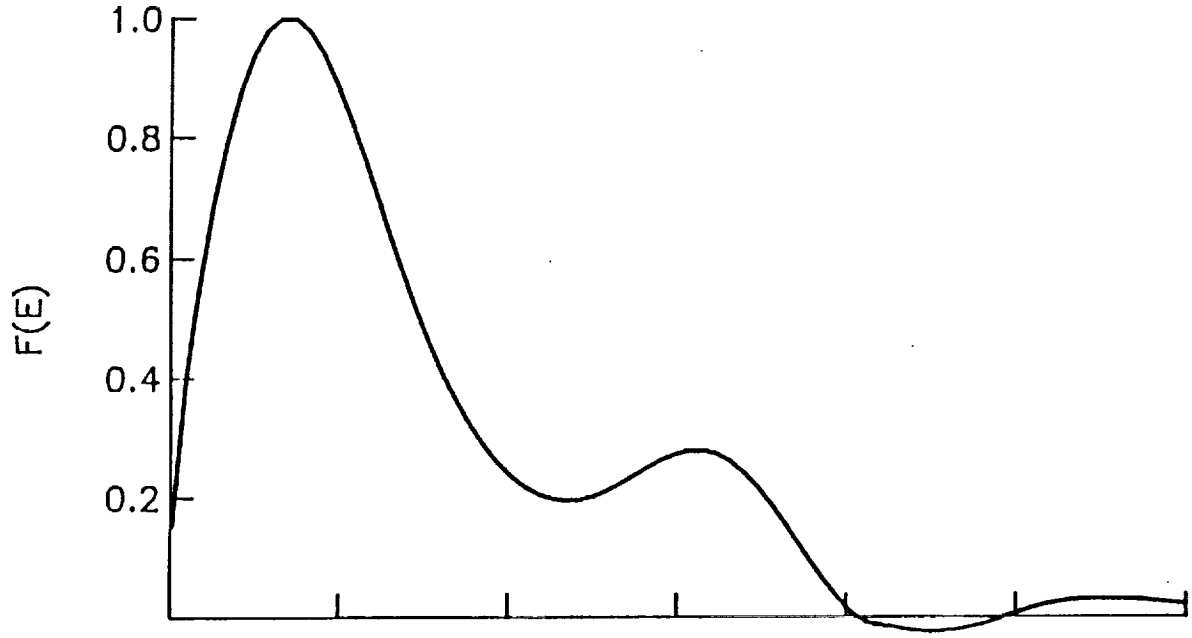

a. Contactor Plasma Cloud Data

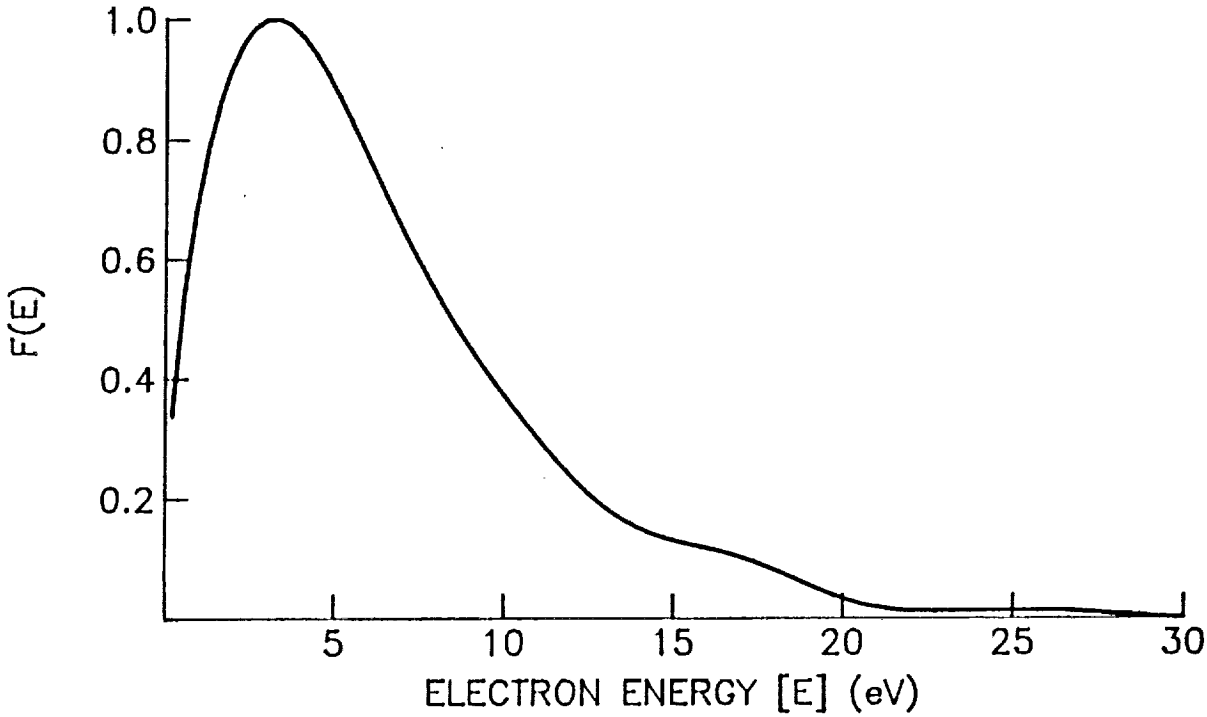

b. Ambient Plasma Data

Fig. A2 Electron Energy Distributions Calculated from the Langmuir Probe Traces Shown in Fig. A1

Conclusions

The distribution functions obtained by computing the second derivative of experimental Langmuir probe traces are typically too noisy to be of any value, however, they can be made less noisy through the use of a Lanczos convergence factor in conjunction with a sine series fit. The use of the Lanczos convergence factor is equivalent to smoothing the experimental data, and it causes smoothing errors. In addition, errors caused by inaccuracies in plasma potential measurements and natural rounding of the Langmuir probe trace near plasma potential in a noisy plasma probably introduce some inaccuracies into the electron distributions functions. Although errors reduce the accuracy of the computed distribution functions, the procedure outlined here does provide useful, qualitative estimates of electron energy distributions.

Appendix B

PLASMA POTENTIAL MEASUREMENTS IN LOW DENSITY PLASMAS USING AN EMISSIVE PROBE

Experiments were conducted at CSU, LeRC and IFSI-CNR to investigate the accuracy of plasma potentials measured in low density plasmas using emissive probes. The LeRC vacuum system in which the most extensive tests were conducted and the electrical circuits that were used to power the probe and plasma source system are shown schematically in Fig. B1. Typical tests were initiated by striking a discharge within the ion source and allowing the plasma which it produces to expand into the chamber. The characteristics of the plasma were studied with an emissive probe that was fixed at radial and axial coordinates of ~ 0.7 m and ~ 1.2 m, respectively, from axes defined by the ion source/facility centerline and the source aperture.

The ion source is a simple, divergent field discharge chamber which is equipped with a hot filament cathode. One side of the cathode was connected to the tank wall and the ion source body (which also serves as the anode) was biased 50 V positive of the cathode using the anode supply shown in Fig. B1. The discharge current (J_A) flowing from the cathode to the body was controlled by adjusting the cathode filament temperature using the heater supply (i.e. by adjusting J_{DF}). The source was operated on argon for all tests.

The emissive probe is constructed from tungsten wire (76 μm dia. and ~ 1.2 cm long) formed into a semi-loop with its ends attached to lead wires via low resistance contacts which are insulated from the plasma using ceramic adhesive. The high power potentiometer shown in Fig. B1 could be used to adjust the heating current (J_H) over a

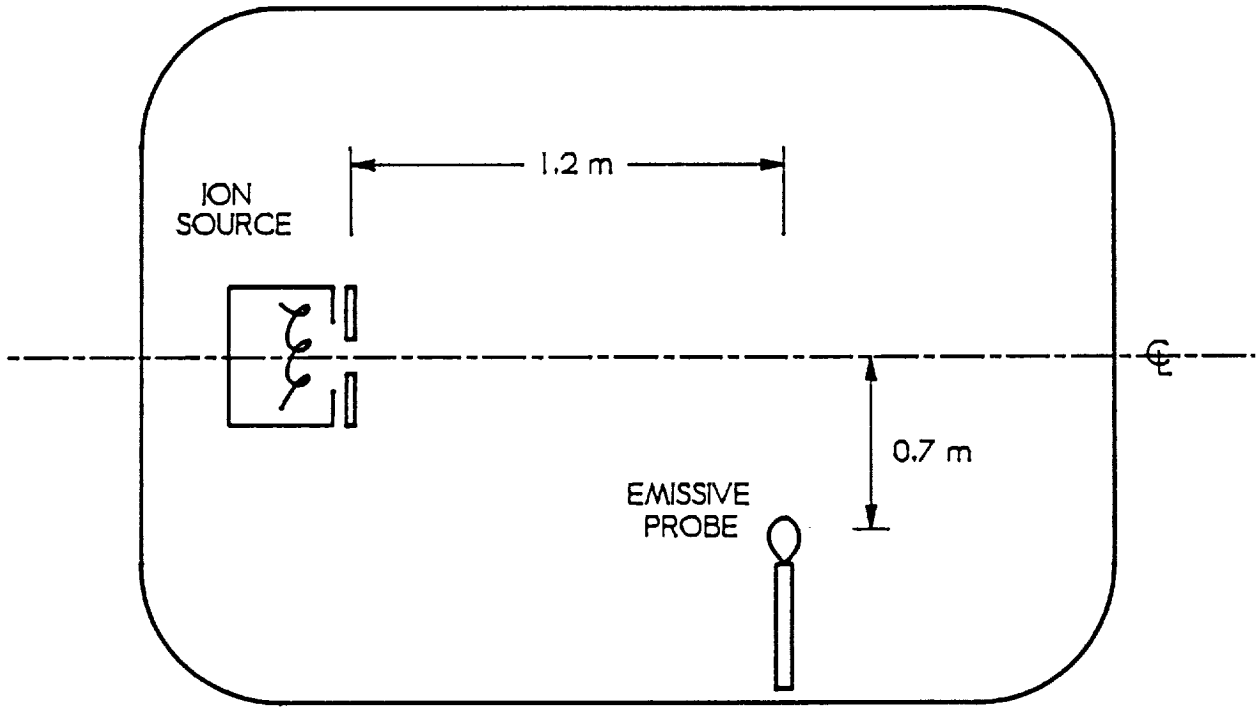

PHYSICAL SETUP

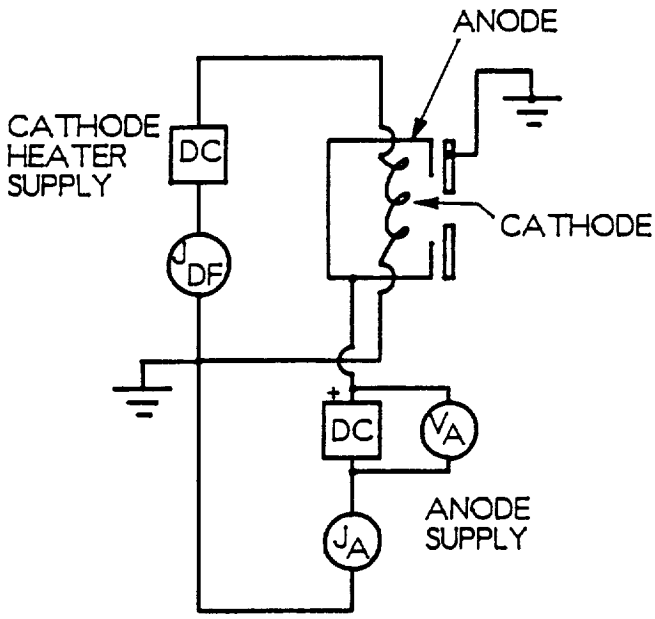

ION SOURCE CIRCUIT

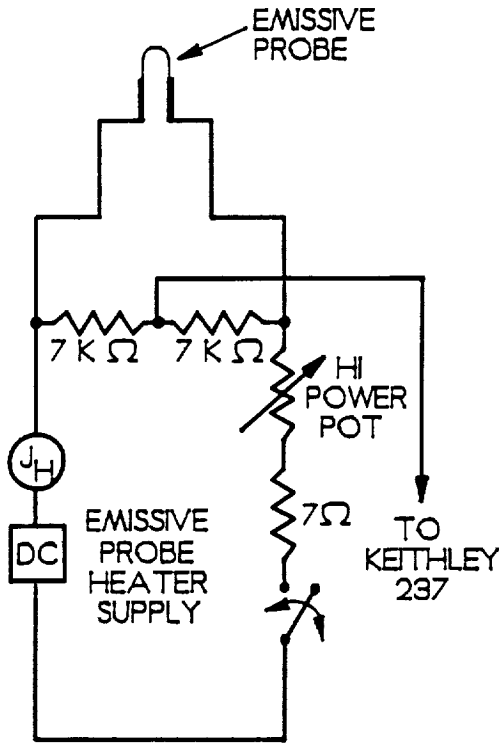

EMISSIVE PROBE CIRCUIT

Fig. B1 NASA Lewis Electrical and Mechanical Schematics

range from 0.5 A to 1.2 A. At the lower limit (0.5 A) the filament appeared dark to the naked eye, while it appeared white hot at currents over 0.9 A. A typical incandescent light bulb filament temperature is about 2800 K and this temperature is comparable to the emissive probe temperature at the higher heating currents. The potential of the common point between the precision 7 kΩ resistors could be varied using a Keithley 237 electrometer and voltage source, and the electron current collected by the emissive probe could be measured as a function of this potential. Note that the Keithley 237 power supply sees an input impedance due to the two precision resistors and the effective impedance between the emissive probe and the plasma in which it is immersed. When the emissive probe is cold and is in a relatively low density, low temperature plasma, the effective impedance between the probe and the plasma is very high compared to 3.5 kΩ--the effective impedance to the probe through the precision resistors. Consequently, the effect of the precision resistors on the current/voltage characteristic is small and can be neglected. However, when the emissive probe is heated white hot and is biased negative with respect to the plasma, its effective impedance to the plasma decreases. At this condition the precision resistors can affect the probe current/voltage characteristics by limiting the electron emission current to the surrounding plasma.

Several current/voltage characteristic curves obtained using the emissive probe are shown in the upper plot of Fig. B2. They were measured at heating currents (J_H) of 0.5, 0.8, 0.9, and 1.1 A when the ion source was being operated on argon at an anode current and voltage of 0.8 A and 50 V, respectively. When the probe was relatively cold ($J_H \approx 0.5$ A), it behaved like a conventional Langmuir probe and the associated probe current/voltage curve could be analyzed to obtain a plasma potential of

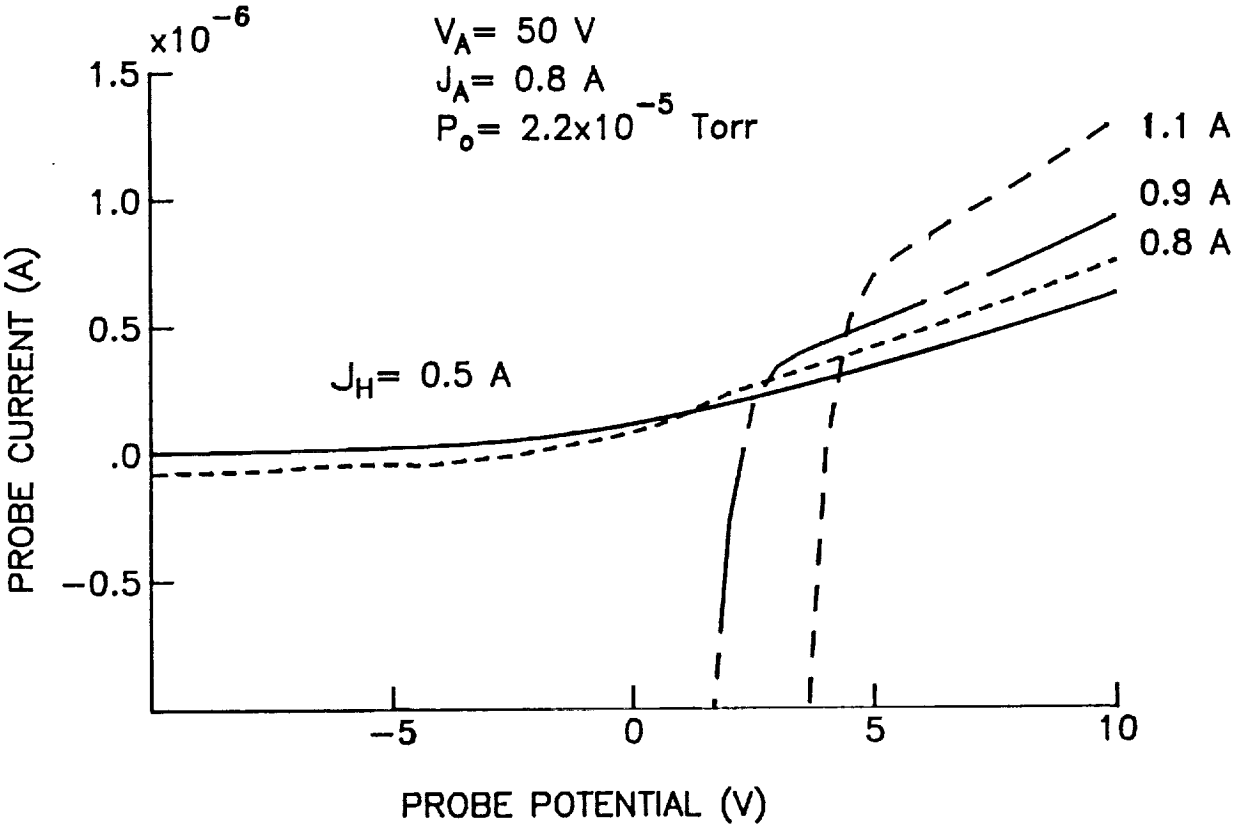

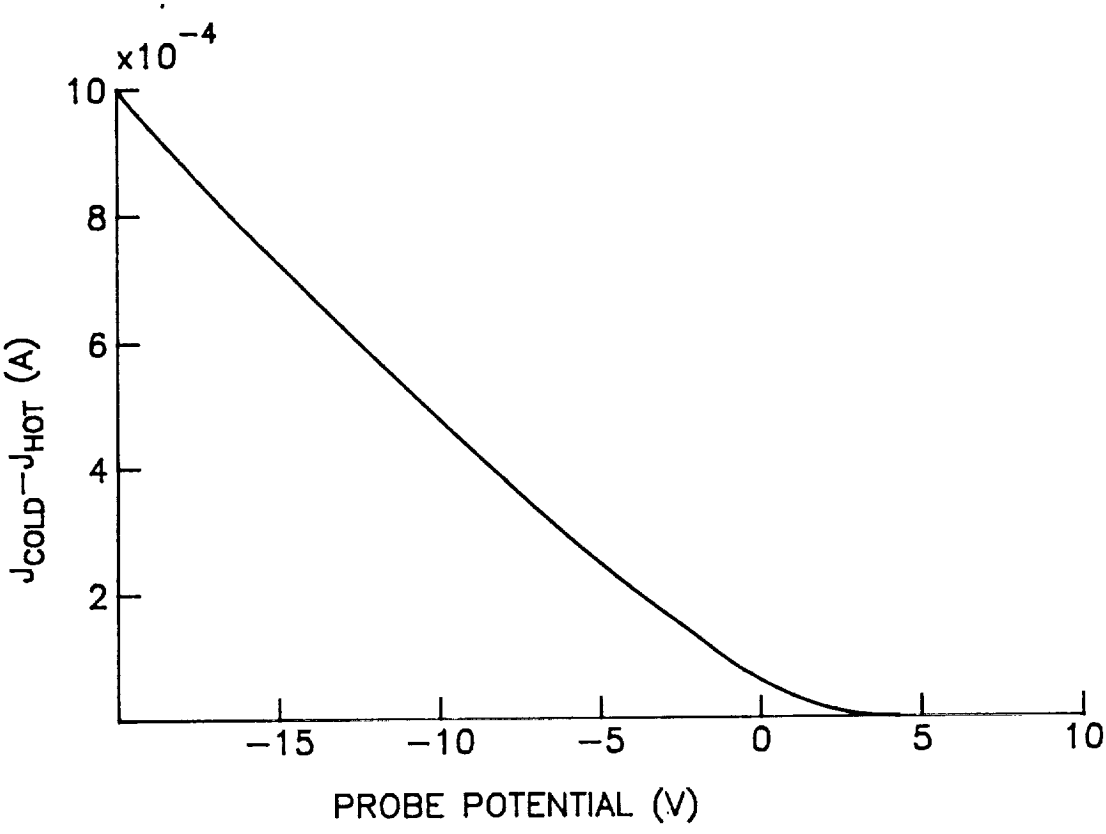

Fig. B2 Effect of Heating Current on Emissive Probe Current/Voltage Traces

3.8 V, a plasma density of 2.1×10^6 cm^{-3}, and an electron temperature of 3.1 eV. The pressure in the facility during this test ($P_o = 2.2 \times 10^{-5}$ Torr) was determined by multiplying the value read from an ionization pressure gauge by the appropriate correction factor (0.66 for argon).

As an emissive probe is heated to higher temperatures and held below plasma potential, it emits a progressively greater electron current. For example, the upper plot in Fig. B2 shows that increasing the heating current from 0.8 to 1.1 A causes the probe current measured below plasma potential to change from zero to large negative values. The bottom plot in Fig. B2 was constructed by subtracting the curve labelled $J_H = 1.1$ A from the one labelled 0.5 A. This plot shows that the emission current from the white hot probe increases as the probe is held more negative of plasma potential and that it does not saturate. Previous experiments conducted at CSU in higher density plasmas showed that the emission current does saturate and the reason it did not saturate in the Lewis tests is not understood. Possible explanations for this difference include a) higher neutral densities in the Lewis facility which enhanced ion production near the probe and facilitated increased ion collection by the probe as it was biased more negative and b) limitations imposed by the 7 kΩ precision resistors on the emission capabilities of the hot probe. The effective impedance associated with operation of the hot probe at potentials below about 0 V in Fig. B2 is simply the reciprocal of the absolute value of the slope over this same potential region. This turns out to be ~20 kΩ, which is about an order of magnitude greater than the effective impedance associated with the precision resistors (3.5 kΩ). This result indicates that the effective impedance of the precision resistors should have a negligible effect on the current\voltage characteristic curve. It can be concluded from the data of Fig. B2 that

the actual emission characteristics of a hot emissive probe are highly dependent on the probe temperature and the properties of the plasma in which it is immersed. A model that describes probe emission characteristics like those in Fig. B2 would have to account for both of these effects.

The characteristic curves shown in the top plot of Fig. B2 also differ at potentials above plasma potential--namely, the hotter probes collect greater electron currents. It is noted that the emissive probe temperature at the highest heating current is only about 3000 K so it should be unable to emit electrons when it is at any potential greater than about 0.3 volts above plasma potential. Consequently, all of the curves in the upper plot of Fig. B2 should fall on top of one another at potentials about 0.3 V above plasma potential. Several phenomena could induce the systematic probe temperature-related increase in electron current to the filament from the plasma at potentials beyond this value. Specifically, increases in probe temperature could induce: a) physical growth of the probe surface area, b) growth of the effective probe collection area as a result of increased conductivity of the insulating surface in contact with the probe wire and c) increased rejection of contaminants from the probe surface. Detailed evaluation of each of these possibilities suggests:

a) The linear thermal expansion coefficient for tungsten when it is heated from 293 K to 3000 K is about 1.6% [18]. If the tungsten wire expands in both length and diameter by this amount the surface area only increases by 2.7%. Conclusion- effect is negligible.

b) The ceramic adhesive used at CSU is Ceramabond 569 and it has been found to become increasingly conductive as its temperature is increased above $\sim$400 K. Depending on how quickly heat is conducted away from the ceramic adhesive in contact with the emissive probe, it is possible that some ceramic will become sufficiently conductive to increase the effective area of the probe exposed to the plasma as probe temperature is increased. Conclusion- effect is a possible contributor to observed error.

c) Contamination was observed on large Langmuir probes which were located in the facility during the three days of testing. However, analysis of the cold characteristic curve for the emissive probe indicated a plasma potential close to the point where the hotter curves begin to display electron emission. This agreement suggests that the contamination layer resistance at cold probe temperatures is not significant compared to the impedance between the probe and the plasma. Conclusion- effect is not considered to be substantial for the low density and temperature plasmas being investigated.

It is also possible that plasma conditions varied as probe heating current was changed but such changes would be expected to be random rather than systematic. The data in the upper plot of Fig. B2 show a systematic change in probe current with heating current so this is considered an unlikely explanation.

Figure B3 is a plot of floating potential versus emissive probe heating current corresponding to the data shown in Fig. B2. The floating potentials were measured by noting the potential where the current sensed by the Keithley 237 was zero and they are shown to remain at about -10.7 V until the heating current is about 0.7 A. At heating currents above 0.7 A, the floating potential rises quickly and appears to saturate at a value between 4 and 4.6 V. This number is in reasonable agreement with the value obtained for the plasma potential from the Langmuir probe analysis program (3.8 V). Consequently, Fig. B3 suggests that the emissive probe is performing properly and that its floating potential at high heating currents is a good indication of plasma potential.

In order to change the plasma density at the emissive probe location, the ion source discharge (anode) power was varied. Figure B4 shows the effects of changes in anode current (J_A) on the plasma density and plasma potential sensed by the emissive probe. One important observation that can be made from the data shown at the top of Fig. B4 is that the plasma density varies linearly with anode current. Note that the anode voltage (V_A) was held constant at 50 V so discharge power should be directly

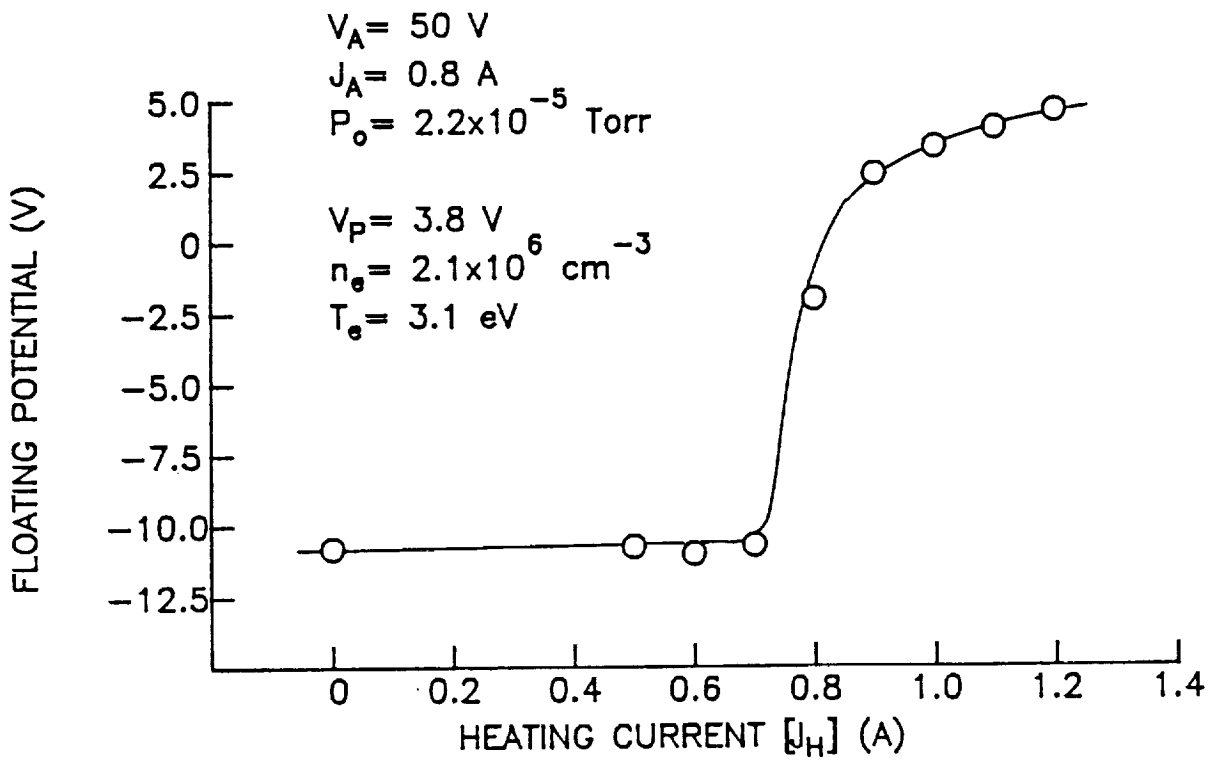

Fig. B3 Effect of Heating Current on Emissive Probe Floating Potential

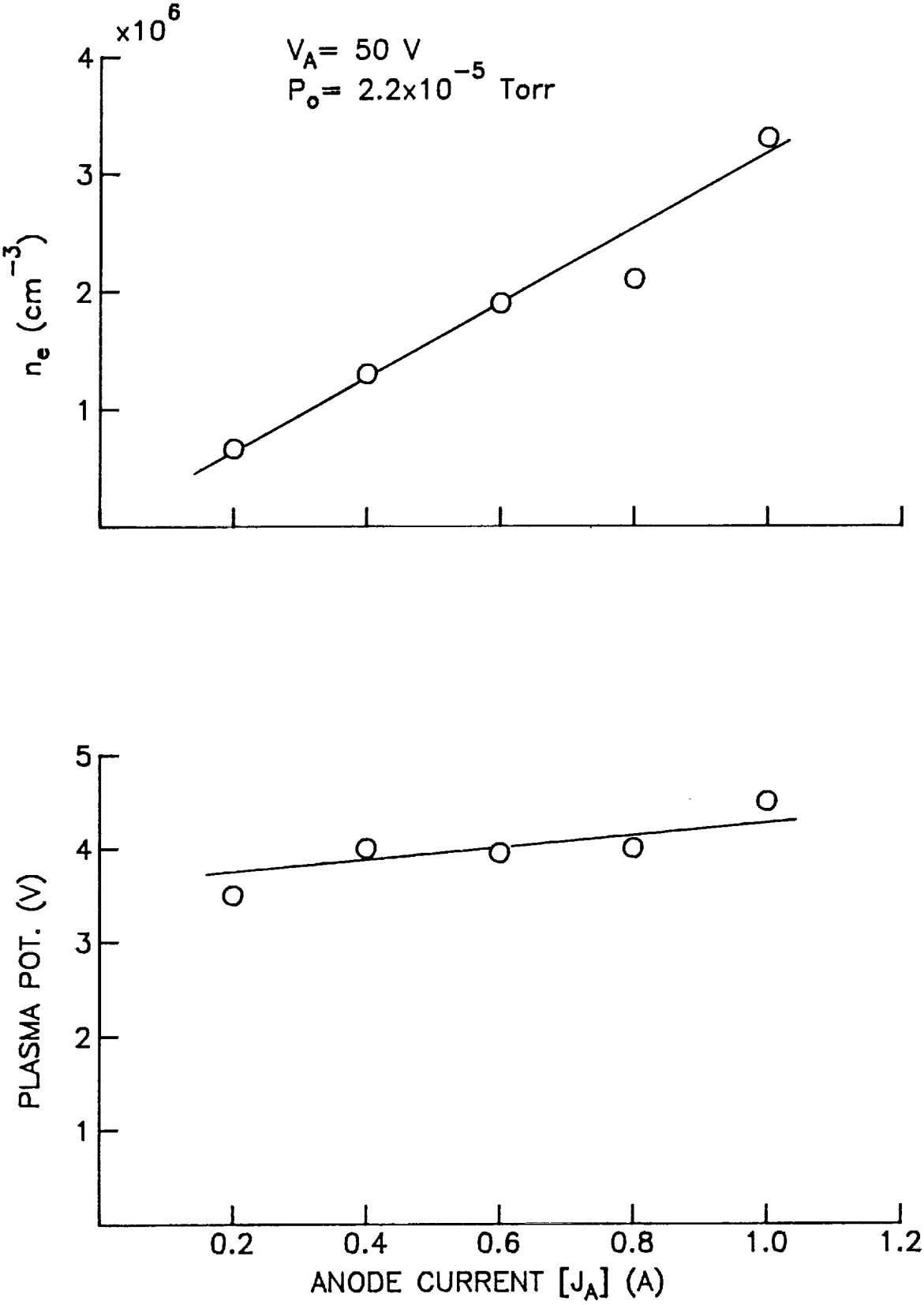

Fig. B4 Application of Emissive Probe: Effect of Anode Current on Plasma Density and Potential

proportional to the anode current for these curves. This suggests that plasma density in the vicinity of the emissive probe is linearly proportional to ion source discharge power. The electron temperature was found to be relatively constant at about 3 eV over the range of anode currents shown in Fig. B4. The bottom plot in Fig. B4 shows that the plasma potential was also relatively constant at about 4 V.

The plasma produced within the ion source should have a potential near the source anode potential and electrons and ions created in the source should be drawn from this potential into the facility. The plasma potential in the facility should adjust itself so that the rates of ion and electron loss from it will match the rates of ion and electron supply from the source. This potential should be negative of the source plasma and positive of the tank wall so electric fields in sheaths near the tank wall can allow most ions to flow to and most electrons to be repelled from the tank walls. Under these conditions ions would be accelerated and energetic electrons would be decelerated (and cooled) as they travel from the interior of the source to the facility.

DISTRIBUTION LIST

	Copies
National Aeronautics and Space Administration Washington, DC 20546 Attn:	
Ms. Pat Conners, Code MD	1
Mr. Thomas D. Stuart, Code MK	1
Dr. Stanley Shawhan, Code ES	1
Dr. L.R. Owen Storey, Code ES	1
Mr. George Levine, Code MTF	1
Mr. Ivan Bekey, Code Z	1
Mr. John L. Anderson, Code RS	1
National Aeronautics and Space Administration Lewis Research Center 21000 Brookpark Road Cleveland, OH 44135 Attn:	
Technology Utilization Office, MS 7-3	1
Report Control Office, MS 60-1	1
Library, MS 60-3	2
Dr. M. Goldstein, Chief Scientist, MS 5-9	1
Mr. Dave Byers, MS 500-219	1
Mr. Vincent Rawlin, MS 500-220	1
Mr. Joseph C. Kolecki, MS 302-1	1
Mr. Michael Patterson, MS 500-220	1
Dr. Dale Ferguson, MS 302-1	1
Dr. Barry Hillard, MS 302-1	1
Dr. Willie Mackey, MS 302-1	1
Mr. Norman T. Grier, MS 302-1	1
Mr. Joel T. Galofaro, MS 302-1	10
National Aeronautics and Space Administration Lyndon B. Johnson Space Center Houston, TX 77058 Attn:	
Dr. James E. McCoy, Mail Code SN3	1
National Aeronautics and Space Administration Marshall Space Flight Center Huntsville, AL 35812 Attn:	
Mr. J. H. Laue, Mail Code FA31	1
Mr. Chris Rupp, Mail Code PS04	1
Mr. James K. Harrison, Mail Code PS04	1

	Copies
NASA Scientific and Technical Information Facility P.O. Box 8757 Baltimore, MD 21240 Attn: Accessioning Dept.	1
Dept. of the Navy Office of Naval Research University of New Mexico Bandolier Hall West Albuquerque, NM 87131 Attn: G. Max Irving	1
Procurement Executive, Ministry of Defense Royal Aircraft Establishment Farnborough, Hants GU14 6TD ENGLAND Attn: Dr. D. G. Fearn	1
United Kingdom Atomic Energy Authority Culham Laboratory Abingdon, Oxfordshire OX143DB ENGLAND Attn: Dr. A. R. Martin (Rm F4/135)	1
SRT Technologies 1500 Wilson Blvd, Suite 800 Arlington, VA 22209-2415 Attn: Ms. Kaye Anderson	1
Jet Propulsion Laboratory 4800 Oak Grove Laboratory Pasadena, CA 91109 Attn:	
Technical Library	1
Dr. John R. Brophy	1
Dr. Paul Penzo, Code 1156-217	1
Dr. Stephen Gabriel	1

	Copies
TRW Inc. TRW Systems One Space Park Redondo Beach, CA 90278 Attn:	
Dr. Rob Stillwell	1
National Aeronautics and Space Administration Ames Research Center Moffett Field, CA 94035 Attn:	
Technical Library	1
National Aeronautics and Space Administration Langley Research Center Langley Field Station Hampton, VA 23365 Attn:	
Technical Library	1
Mr. Dick Deloach, Mail Code 234	1
Hughes Research Laboratories 3011 Malibu Canyon Road Malibu, CA 90265 Attn:	
Dr. Jay Hyman, MS RL 57	1
Dr. J. R. Beattie, MS RL 57	1
Dr. J. N. Matossian, MS RL 57	1
Mr. Lee Parker 252 Lexington Road Concord, MA 01741	1
Department of Aeronautics and Astronautics Massachusetts Institute of Technology Cambridge, MA 02139 Attn:	
Dr. Daniel E. Hastings, Rm 37-441	1
Institute for Space and Aeronautical Science 4-6-1 Komaba, Meguro-ku, Tokyo, 153, JAPAN Attn:	
Prof. K. Kuriki	1
Prof. T. Obayashi	1

	Copies
Tokai University Kitakauame, Hiratsuka, Kanagawa, JAPAN Attn: Prof. K. Hirao	1
Physics Department Naval Postgraduate School Monterey, CA 93943-5000 Attn: Dr. Chris Olson, Mail Code 61-0S	1
Martin Marietta Aerospace P. O. Box 179 Denver, CO 80201 Attn: Dr. L. Kevin Rudolph, MS S8064	1
S-Cubed P. O. Box 1620 LaJolla, CA 92038 Attn: Dr. Ira Katz Dr. Victoria A. Davis	1 1
Electric Propulsion Laboratory, Inc. 43423 N. Division St., Suite 205 Lancaster, CA 93535 Attn: Dr. Graeme Aston	1
Mr. Joe Carroll Energy Science Laboratories, Inc. P.O. Box 85608 San Diego, CA 92138-5608	1
Science Applications International Corp. 13400 B Northrop Way #36 Bellevue, WA 98005 Attn: Dr. Hugh Anderson	1

	Copies
Istituto di Fisica dello Spazio Interplanetario Consiglio Nazionale delle Ricerche Via G. Galilei 00044 Frascati, ITALY Attn:	
Dr. Marino Dobrowolny	1
Dr. Carlo Bonifazi	1
Dr. Luciano Iess	1
Dr. Giuliano Vannaroni	1
Starlab/SEL Stanford University Stanford, CA 94305 Attn:	
Dr. Peter Banks	1
Dr. Roger Williamson	1
Science Applications International Corp. Plasma Physics Division 1710 Goodridge Drive McLean, VA 22102 Attn:	
Mr. Edward P. Szuszczewicz	1
University of Alabama (Huntsville) Electrical and Computer Engineering Dept. Engineering Building Huntsville, AL 35899 Attn:	
Dr. Michael Greene	1
Physics Department Utah State University Logan, Utah 84322 Attn:	
Dr. W.J. Raitt	1
Grumman Corp. 420 Wynn Dr. Huntsville, AL 35805 Attn:	
Dr. Kai-Shen Hwang	1

	Copies
Dr. Roy Torbert Space Science Center Rm. 406 University of New Hampshire Durham, NH 03824	1
Institut f. Geophysik u. Meteorology Albertus-Magnus-Platz D-5000 Köln 41 West Germany Attn: Mr. Hartmut Marschall	1
Capt. Lon Enloe GL(AFSC)/PHP Hanscom AFB, MA 01731-5000	1